

## Climate Model Forecast Experiments for TOGA COARE

J. BOYLE AND S. KLEIN

*Lawrence Livermore National Laboratory, Livermore, California*

G. ZHANG

*Scripps Institute of Oceanography, La Jolla, California*

S. XIE

*Lawrence Livermore National Laboratory, Livermore, California*

X. WEI

*University of Colorado and NOAA/Earth System Research Laboratory, Boulder, Colorado*

(Manuscript received 17 January 2007, in final form 17 June 2007)

### ABSTRACT

Short-term (1–10 day) forecasts are made with climate models to assess the parameterizations of the physical processes. The time period for the integrations is that of the intensive observing period (IOP) of the Tropical Ocean Global Atmosphere Coupled Ocean–Atmosphere Response Experiment (TOGA COARE). The models used are the National Center for Atmospheric Research (NCAR) Community Climate Model, version 3.1 (CAM3.1); CAM3.1 with a modified deep convection parameterization; and the Geophysical Fluid Dynamics Laboratory (GFDL) Atmospheric Model, version 2 (AM2). The models were initialized using the state variables from the 40-yr ECMWF Re-Analysis (ERA-40).

The CAM deep convective parameterization fails to demonstrate the sensitivity to the imposed forcing to simulate precipitation patterns associated with the Madden–Julian oscillations (MJOs) present during the period. AM2 and modified CAM3.1 exhibit greater correspondence to the observations at the TOGA COARE site, suggesting that convective parameterizations that have some type of limiter (as do AM2 and the modified CAM3.1) simulate the MJO rainfall with more fidelity than those without. None of the models are able to fully capture the correct phasing of westerly wind bursts with respect to precipitation in the eastward-moving MJO disturbance. Better representation of the diabatic heating and effective static stability profiles is associated with a better MJO simulation.

Because the models' errors in the forecast mode bear a resemblance to the errors in the climate mode in simulating the MJO, the forecasts may allow for a better way to dissect the reasons for model error.

### 1. Background

For the purpose of validating the parameterizations used in climate models, the models are used to produce weather forecasts. Over the course of a short-term forecast (e.g., 3–10 days) the errors emerging from individual parameterizations are not as intertwined as in a long climate simulation, and thus a source of trouble might be more apparent. The forecast might also shed

light on the etiology of the climate biases if these manifest themselves in the short integration. The utility of a short-term forecast to diagnose errors requires that the model be started from as realistic conditions as possible. Deviations of the model forecasts from the subsequent observed weather can be documented and the causes diagnosed in a manner more transparent than in a statistical evaluation of a climate simulation.

The model integrations are run over the intensive observing period (IOP) of the tropical Ocean Global Atmosphere Coupled Ocean–Atmosphere Response Experiment (TOGA COARE), which spanned the period from 1 November 1992 to 28 February 1993. This

---

Corresponding author address: J. Boyle, Lawrence Livermore National Laboratory, 7000 East Ave., Livermore, CA 94550.  
E-mail: boyle5@llnl.gov

time period is rich in varied tropical phenomena (Gutzler et al. 1994) and has a comprehensive amount of observational data. Many aspects of the TOGA COARE period have been studied extensively, permitting a useful framework for model verification. Intraseasonal variability was quite pronounced during the IOP. This afforded examples of the Madden–Julian oscillation (MJO) and the wind bursts embedded within them (Lin and Johnson 1996). In this work extensive use will be made of the observations taken on the Intensive Flux Array (IFA) of TOGA COARE centered at about 2°S, 155°E.

The well-documented MJO activity occurring during the TOGA COARE IOP affords a critical evaluation of the models' parameterizations driven by this very important form of tropical variability. The MJO is a convectively coupled and highly viscous Kelvin–Rossby wave, which moves along the equator eastward from the Indian Ocean to the date line with a phase speed of about 5–10 m s<sup>-1</sup> (Lin et al. 2006). The MJO is the dominant tropical intraseasonal mode, but its poor simulation is endemic among general circulation models (Slingo et al. 1996; Lin et al. 2006). Generally, the oscillations tend to be too weak and too fast in those models where they have some signal. Previous modeling studies indicated that the MJO depiction is sensitive to the representation of convection. Slingo et al. (1996) indicates that those models with CAPE closure tended to be more realistic. It was also found that adding moisture triggers to the convective schemes aided the MJO signal. The vertical profile of diabatic heating could also be significant in driving MJO variability (Lin et al. 2004). The forecast framework permits the evaluation of many aspects of the model in the context of observed MJO dynamic forcing.

The structure of the paper is as follows: The next section will present the climate models used. This will be followed by the experimental design. Section 4 documents the verification data, which is cited, and this is followed by the presentation of the results. The paper's conclusions are presented in the final section.

## 2. Models used

Since this study is focused on short time-scale processes in the tropics, the convective parameterizations of each model will be the only aspect to be described in any detail.

### a. NCAR Community Atmosphere Model, version 3.1 (CAM3.1)

The unmodified CAM, version 3.1, of Collins et al. (2004) was used in this study. The model was run using

the Eulerian spectral dynamics with a spectral resolution of T42 and 26 vertical levels (L26) or 30 vertical levels (L30). The deep convection parameterization uses the convective available potential energy (CAPE)-based closure described by Zhang and McFarlane (1995). The scheme is based on a plume ensemble approach, where it is assumed that an ensemble of convective scale updrafts (and the associated saturated downdrafts) may exist whenever the atmosphere is conditionally unstable in the lower troposphere. The closure condition assumes that deep convection acts to consume CAPE within a fixed relaxation time of 2 h. The cloud-base mass flux is directly proportional to the value of CAPE at each grid point. The scheme is triggered if CAPE exceeds 70 J kg<sup>-1</sup>. CAM also has a parameterization to characterize the convective forcing associated with shallow and midlevel convection, which is not treated by the deep convection scheme. For convenience, this shallow/middle convection parameterization will be referred to as the Hack scheme (Hack 1994).

### b. CAM convection parameterization modification

The modification to the Zhang–McFarlane (ZM scheme) deep convection parameterization described by Zhang and Mu (2005) was implemented in the CAM3.1, T42 L26 run. Hereinafter this modified version will be referred to as ZMO. The closure of the modified scheme assumes the cloud-base mass flux is proportional to the CAPE change due to the temperature and moisture changes above the boundary layer that result from the large-scale processes. In this case the free troposphere is the region above the boundary layer. The modified scheme includes a relative humidity threshold as a convection trigger to suppress convection in conditions when the boundary layer is too dry. The relative humidity of the air at the parcel lifting level must be greater than 80% for deep convection to occur. Additionally, the new scheme allows convection initiating above the PBL top to be included in the deep convective parameterization. In the default CAM, this upper-level instability is for the most part addressed by the Hack convection parameterization. The Hack scheme itself is unmodified from the default CAM formulation.

### c. GFDL Atmospheric Model (AM2)

The Geophysical Fluid Dynamics Laboratory AM2 (GFDL Global Atmospheric Model Development Team 2004) was run in the “bgrid” (2.0° × 2.5°) configuration with 24 vertical levels. The AM2 cumulus parameterization is a relaxed Arakawa–Schubert for-

mulation (Moorthi and Suarez 1992). Closure is determined by relaxing the cloud work function for each cloud type in the spectrum back to a critical value over a fixed time scale. The cloud work function is reduced to zero for shallow updrafts that detrain below 600 hPa. Deep convection is prevented in updrafts with a lateral entrainment rate lower than a critical value determined by the depth of the subcloud layer (Tokioka limiter; Tokioka et al. 1988). This entrainment limiter is only applied to deep convection (tops above 500 hPa). Use of this limiter increases the amplitude of tropical transient activity to bring it closer to observed values. In the AM2 implementation of the relaxed Arakawa–Schubert, there are no parameterized down-drafts.

Convective momentum transport (CMT) is parameterized by a downgradient diffusive formulation. The impact of cumulus convection on the horizontal momentum is represented by adding to the vertical diffusion coefficient for momentum a term directly proportional to the cumulus mass flux and depth of convection. The current (3.1) version of CAM does not have any parameterization of cumulus momentum transport.

### 3. Experiment design

#### a. Initialization

The availability of high-quality analyses from numerical weather prediction (NWP) centers affords an excellent starting point for providing initial data to the climate model. The crucial path is that of taking the analyses that are in balance for the model used in the data assimilation and producing data that is in near balance for the climate model yet as near to the observed atmosphere as possible.

The models were initialized using the state variables (winds, temperature, specific humidity, and surface pressure) from the 40-yr European Centre for Medium-Range Weather Forecasts (ECMWF) Re-Analysis (ERA-40; Uppala et al. 2005). The ERA-40 data were on the original  $\eta$  normalized pressure coordinates (60 levels) and were interpolated to the model  $\eta$  coordinates using procedures based on the ECMWF “full pos” procedures (White 2002), which are used for initializing the ECMWF models using data from other assimilation systems. The methods employed here mimic the forecast analysis cycle of the NWP centers. At the centers, the analyses are carried out every 6 h using all the observations available. A 6-h forecast from the previous analysis time supplies the new background for the analysis variables, and provides updates to model fields that are not analyzed such as prognostic

clouds and land variables. The cycle then proceeds with another 6-h forecast and analysis.

In modern data assimilation systems the state produced by the analysis is usually suitable for the starting point of the 6-h forecast. In the past, the analyzed state was not in balance with the forecast model and techniques, such as the nonlinear normal mode initialization (NNMI), were employed so that the model could produce as good a short-term forecast as possible. Our situation is analogous to the past problems, in that the model we are initializing is neither the model used in the analysis, nor is it on the same horizontal and vertical discretization. This mismatch will result in some initial imbalance.

Fillion et al. (1995) demonstrated that use of a properly designed digital filter (Lynch and Huang 1992) could produce initial states that were actually superior to NNMI for the purpose of model short-term forecasts. The methods of Fillion et al. (1995) were applied to the CAM3.1 forecasts with effective results, in that the technique effectively removed the initial imbalances observed in the first few hours of the integration from the ERA-40 initialized state. These experiments indicated that beyond 24–36 h, the forecast converged to virtually the same solution regardless of the initialization used.

The present work requires different models run on many computer systems. Since the digital filter introduced a complication that had minimal effect on the forecast projections that were of interest (2–3 days), the pragmatic approach was to not use it. Therefore, the only initialization used for the experiments reported here is a careful interpolation to the model grid with a smoothing commensurate with the model horizontal resolution. The results are reported for times beyond 36 h.

The model forecasts are started at 0000 UTC and run for up to 10 days over the TOGA COARE period (1 November 1992–28 February 1993, 120 days). Thus, there are 120 forecasts. Tests indicated that running from other times (0600, 1200, and 1800 UTC) does not affect the results presented here. To generate the time series shown in the figures, chunks of data of 24 h in duration are extracted from each forecast and concatenated to produce a series of data sections starting at a particular forecast projection. Thus the day-3 forecast time series is made up of the 120 forecasts from hours 48 to 72. The model data are saved every time step. Day 3 is used extensively in the results section. This period is selected since it is clear of initialization problems as described above, yet it is close enough to the initial time to expect the model to be reasonably close to the observed atmosphere.

### *b. Specified sea surface temperature*

In this work SSTs are prescribed. The default SSTs are monthly mean values based on observations and linearly interpolated to the required times between values at midmonth. The monthly means used in CAM and AM2 are based on the weekly values of the National Oceanic and Atmospheric Administration (NOAA) optimum interpolation (OI) SST analysis (Reynolds et al. 2002). These weekly data are the highest frequency available suitable for a GCM in the TOGA COARE period. Experiments were carried out comparing the results of using the weekly and monthly SST data input to CAM. The differences between using the two datasets were very small for the analyses carried out in this work. We will present the integrations based on the monthly mean SST.

## 4. Verification data

Extensive surface and upper-level data were available centered at the IFA of TOGA COARE (Johnson and Ciesielski 2000; Ciesielski et al. 2003). The IFA is centered at about  $2^{\circ}\text{S}$ ,  $155^{\circ}\text{E}$ , and spans about  $5^{\circ}$  in latitude and longitude. For rainfall verification three datasets were used. The TOGA COARE IFA budget estimates rain (Johnson and Ciesielski 2000; Ciesielski et al. 2003) and provides good time resolution (6 h), but for a single point. The Climate Prediction Center (CPC) Merged Analysis of Precipitation (CMAP) pentad rainfall (Xie and Arkin 1997) provides global coverage on a  $2.5^{\circ} \times 2.5^{\circ}$  grid, but for 5-day means. The Special Sensor Microwave Imager (SSM/I) rainfall estimates (Wentz and Spencer 1998) are global on a  $0.5^{\circ} \times 0.5^{\circ}$  grid and provide nominal daily data. The SSM/I precipitation estimates are not available over land because of the nature of the retrieval algorithm.

For the state variables outside the IFA location, the data used for verification were the ERA-40 reanalysis (Uppala et al. 2005).

Note that the IFA data used here has had a correction applied to the humidity sounding data, as described by Ciesielski et al. (2003). Ciesielski et al. (2003) maintain that these corrections produce moisture fields free of artifacts due to humidity sensor anomalies. The ERA-40 analysis was carried out using rawinsonde data that were not corrected. Thus, there will be some discrepancy between the IFA and ERA-40 data. Ciesielski et al. (2003) provide an extensive discussion of how these corrections affect the moisture profiles and the variables derived there for the IFA. The possible effects of the difference in rawinsonde data between the IFA and ERA-40 will be discussed

when the variables affected by this difference are presented in the results.

## 5. Results

The presentation of results will expand outward from point data at the IFA to a band about the equator from  $5^{\circ}\text{S}$  to  $5^{\circ}\text{N}$  and finally to the entire tropics. The IFA data allows a detailed examination of many processes in the vertical, but this analysis is confined to a single point. Figure 1 is provided to place the IFA in the context of the larger space–time variability in the tropics during the TOGA COARE IOP. Figure 1 is a time–longitude plot of daily SSM/I rainfall estimates averaged over  $5^{\circ}\text{N}$ – $5^{\circ}\text{S}$ . The missing values, mostly over land, are shaded gray. From about  $100^{\circ}$  to  $130^{\circ}\text{E}$  the Maritime Continent imposes what is probably an artificial minimum due to the presence of some land in the latitude band. Nonetheless, there are two very obvious MJO events that propagate from the Indian Ocean, through the IFA ( $155^{\circ}\text{E}$ ), and proceed to the date line. One begins on about 28 November at  $75^{\circ}\text{E}$  and passes the IFA on about 18 December. The other originates on about 7 January near  $30^{\circ}\text{E}$  and reaches the IFA on about 27 January. There are more localized events at the IFA near 8 December and 6 February.

### *a. IFA*

#### 1) RAINFALL AT IFA

Figure 2 shows the time series of rainfall at the IFA for the observations and the model's day-3 forecasts. The propagating features evident in Fig. 1 contribute to the rain events in the middle of December and January. Figure 1 also indicates that the episodic, locally intense nature of the rain in the larger region is shared by the IFA.

Comparison to observations illustrates that CAM tends to rain less intensely than is observed. The observations are averaged over an area comparable to a model grid cell so the comparison in this sense is fair to the model. Although there are variations, all the observational precipitation datasets point to the CAM systematically underestimating the intensity of rain events. This type of behavior can be linked to the CAPE trigger/closure of the convective scheme. At the IFA the observed values of CAPE (not shown) exceed the threshold specified in the model convective scheme for the entire period. This leads to the persistent rain. The failure of CAPE to be a useful indicator of tropical rainfall has been noted before (McBride and Frank 1999). The scheme is triggered almost every day, and

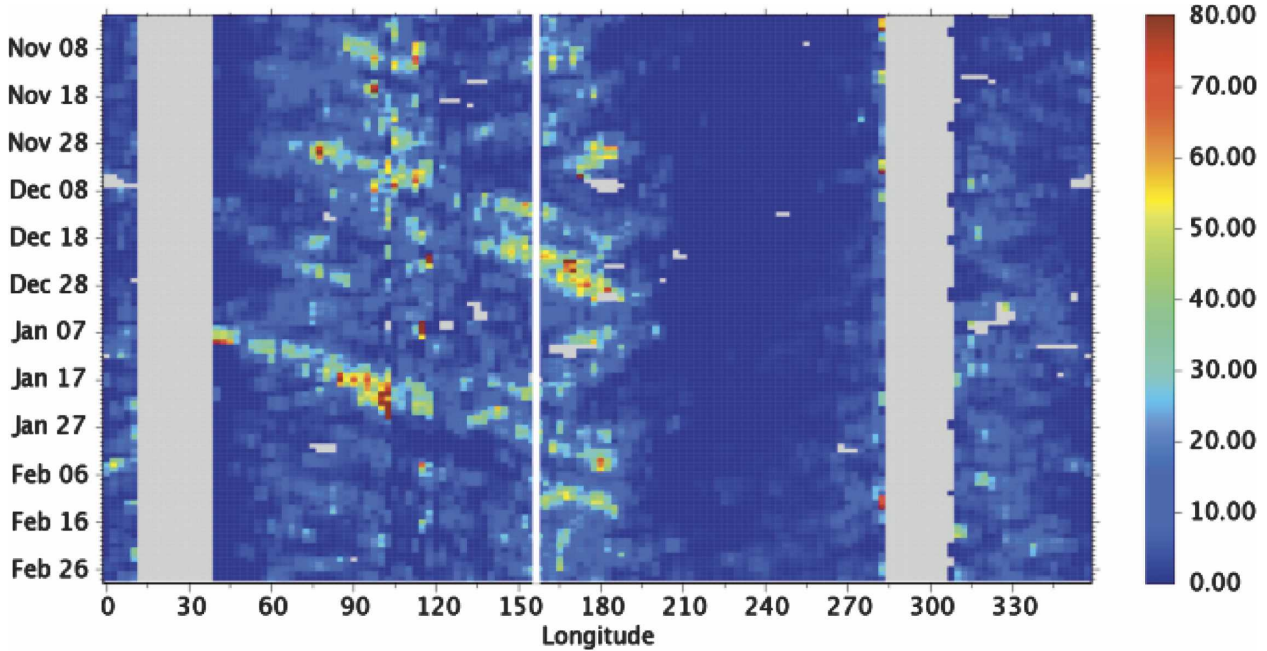


FIG. 1. Time-longitude plot of rainfall estimates ( $\text{mm day}^{-1}$ ) from SSM/I data averaged over  $5^{\circ}\text{N}$ – $5^{\circ}\text{S}$ . Missing data are gray. The retrieval algorithm does not yield values over land. The approximate longitude of IFA is indicated by the white line.

the constant consumption of the available CAPE inhibits a buildup for more explosive events.

ZMO clearly exhibits more intense events than CAM, although these do not always coincide with the observations and ZMO misses some significant events. ZMO's correlation with the observations is 0.27 compared with 0.34 for CAM. The ZMO rainfall is markedly more episodic than that of CAM; the variance is 84 versus  $24 \text{ mm}^2 \text{ day}^{-2}$  for CAM (observed  $55 \text{ mm}^2 \text{ day}^{-2}$ ). This difference in variability is probably due to the restrictions imposed by the RH trigger and using the large-scale forced CAPE changes in place of CAPE trigger of CAM. Experiments made with the RH trigger disabled indicate that its use yields a higher frequency of intense events in the tropics.

The precipitation time series for day 3 of the AM2 forecasts (Fig. 2) has maxima at about the same level as CAM but slightly more defined minima between events. The AM2 variance is  $37 \text{ mm}^2 \text{ day}^{-2}$  and the correlation with the observations is 0.35.

Lin et al. (2006) comment that the Intergovernmental Panel on Climate Change (IPCC) models demonstrating a high level of persistence in the rainfall events tend to do poorly in MJO simulations. Fitting an AR1 model to all the time series in Fig. 2 yields day-1 auto-correlation values of 0.74, 0.82, 0.62, and 0.81 for the observations, CAM, ZMO, and AM2, respectively. Lin et al. (2006) theorize that the use of limiters, such as the

RH trigger in ZMO, can be useful in preventing excessive persistence in modeled rain.

## 2) TEMPERATURE AND MOISTURE AT IFA

Figure 3 presents the time average profiles of the differences of temperature between the ERA-40 and IFA observations and the models' day-3 forecasts. These data are presented for averages over the active, inactive, and entire TOGA COARE periods. The inactive and active periods are listed in Table 1. The periods are chosen subjectively by considering the IFA precipitation (Fig. 2), vertically integrated observed  $Q_1$ , and the observed International Satellite Cloud Climatology Project (ISCCP) deep convective cloud. The active conditions have a substantial contribution from the MJO passages as seen in Fig. 1.

The ERA-40 is the data source from which the models are initialized. There are a number of reasons why the two "observational" data, ERA-40 and IFA, will disagree. The first is that the data assimilation system of ERA-40 has much different techniques and input sources from the IFA analysis. The second is that the ERA-40 analysis is carried out on a vertical and horizontal grid different from the IFA-defined domain. The interpolation methods to put the ERA-40 values onto the IFA-defined region will introduce some differences. The ERA-40 values evaluated in Figs. 3 and 4 are those of a grid with a structure similar to CAM and AM2.

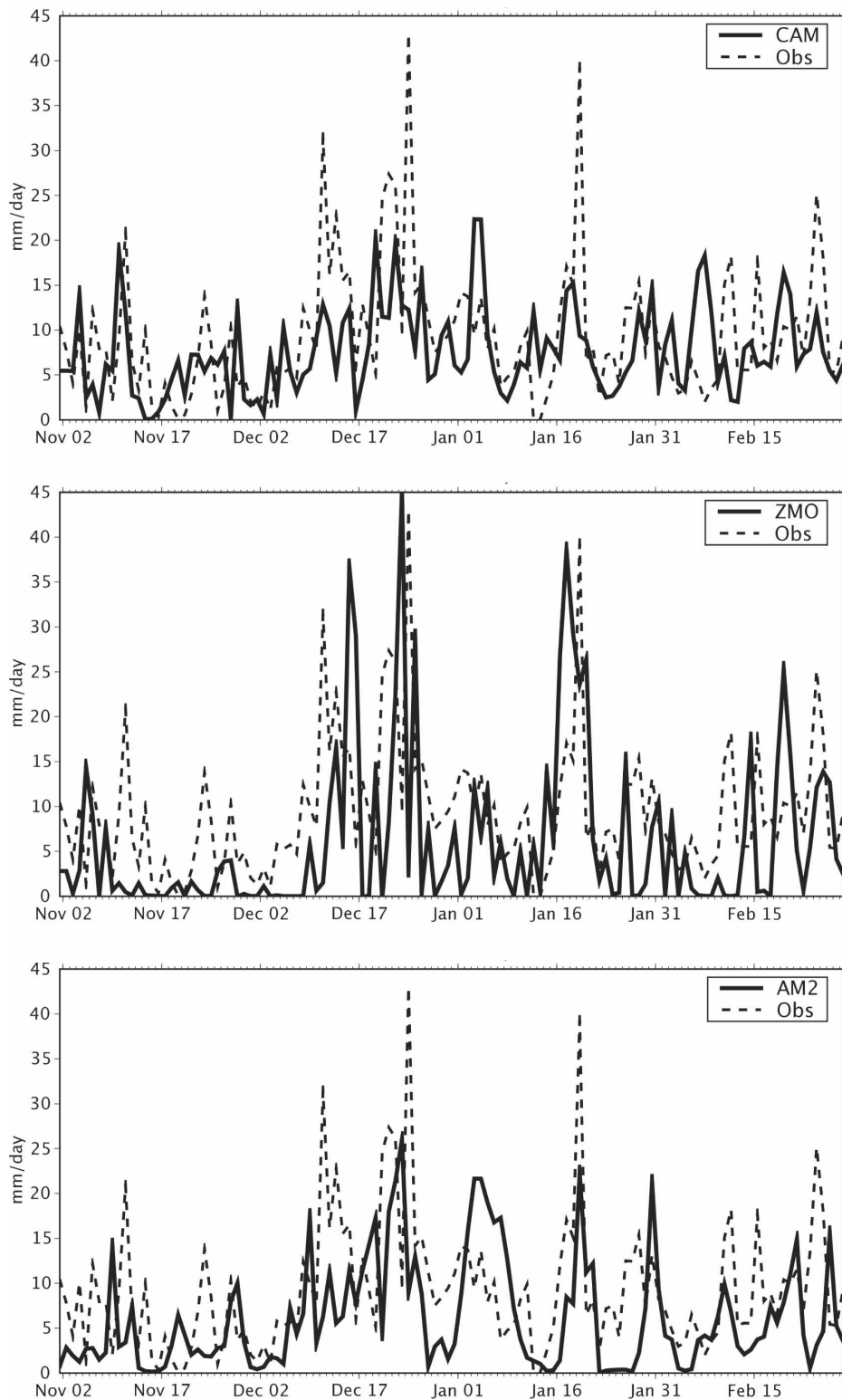


FIG. 2. Rainfall ( $\text{mm day}^{-1}$ ) at the TOGA COARE IFA. Observational estimate from the IFA array budget and (top) CAM forecast day 3, (middle) ZMO forecast day 3, and (bottom) AM2 forecast day 3.

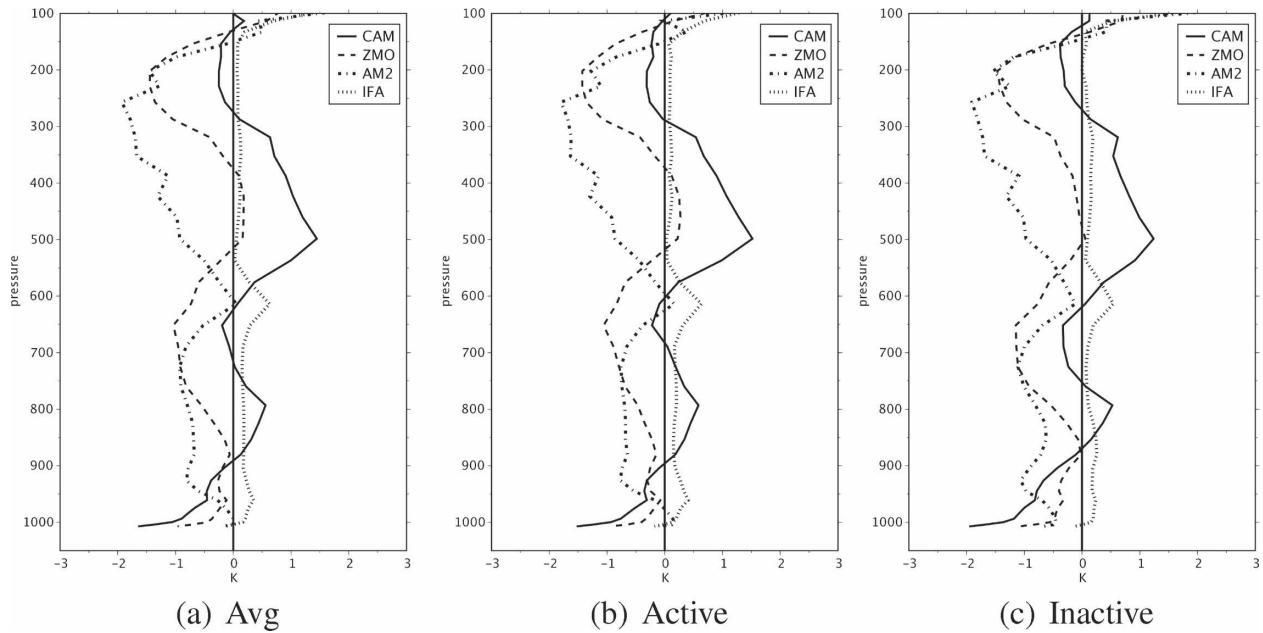


FIG. 3. Profiles of temperature difference (K) from the ERA-40 data for IFA observations and day-3 forecasts of CAM, ZMO, and AM2. Differences are presented for averages over the (a) entire TOGA COARE IOP, (b) active, and (c) inactive periods. The plots all indicate the value of the given data minus the ERA-40 values.

The third reason is that the moisture values for the rawinsonde data have been corrected in the IFA analysis (Ciesielski et al. 2003). The input data for the ERA-40 did not have these corrections. The corrections are only for moisture.

As seen in Fig. 3, IFA is slightly colder than ERA-40. This amounts to about 0.25 K with a bump of 0.5 K at 600 hPa. The 600-hPa feature is near the melting layer ( $0^{\circ}\text{C}$ ) in the IFA region. The temperature differences from ERA-40 (Fig. 3) for the models have very similar shapes across the various averaging periods. It appears that the models establish a characteristic temperature field distinct from the ERA-40, which does not vary rapidly as conditions change. Both CAM and ZMO have similar shapes, but above 900 hPa ZMO has an almost uniform translation with respect to CAM with a cold shift of about a degree. AM2 is more consistently

cold with respect to the ERA-40 through the column. This feature is seen in the AM2 multidecadal climate simulations (GFDL Global Atmospheric Model Development Team 2004). Note that all the models have a cold bias at the upper levels (200 hPa), a defect common to the climates simulated by many GCMs.

Figure 4 is that same as Fig. 3, but the variable is specific humidity. With respect to the ERA-40, the IFA data are moist with respect to ERA-40 with values of about  $1 \text{ g kg}^{-1}$ , and at 800 hPa about  $0.5 \text{ g kg}^{-1}$ , for the average over the whole period. This difference is quite consistent with the corrections presented by Ciesielski et al. (2003). Given that the models start from the ERA-40, the model difference for this variable is calculated as the model minus the ERA-40. The possible shortcomings of ERA-40 still permit a meaningful evaluation of the models. Notice that despite the fact that the differences in the ERA-40 and IFA specific humidity are somewhat larger for the inactive periods, little of this discrepancy is reflected in the model results, indicating that the ERA-40 bias is not dominating the result. In addition, the longer (up to 10 days) model forecast projections show much the same character and magnitude of difference as the shorter forecasts. This is a long enough time that the initial moisture profile has substantially diminished its influence. Generally, the magnitude of the model differences is large enough to establish its nature using either observational set. This

TABLE 1. Time periods used for averaging over the active and inactive times of the TOGA COARE IOP.

Active	Inactive
3–12 Nov 1992	13–21 Nov 1992
22–27 Nov 1992	28 Nov–6 Dec 1992
8–29 Dec 1992	5–16 Jan 1993
15–22 Jan 1993	23–28 Jan 1993
28 Jan–1 Feb 1993	2–9 Feb 1993
10–21 Feb 1993	—

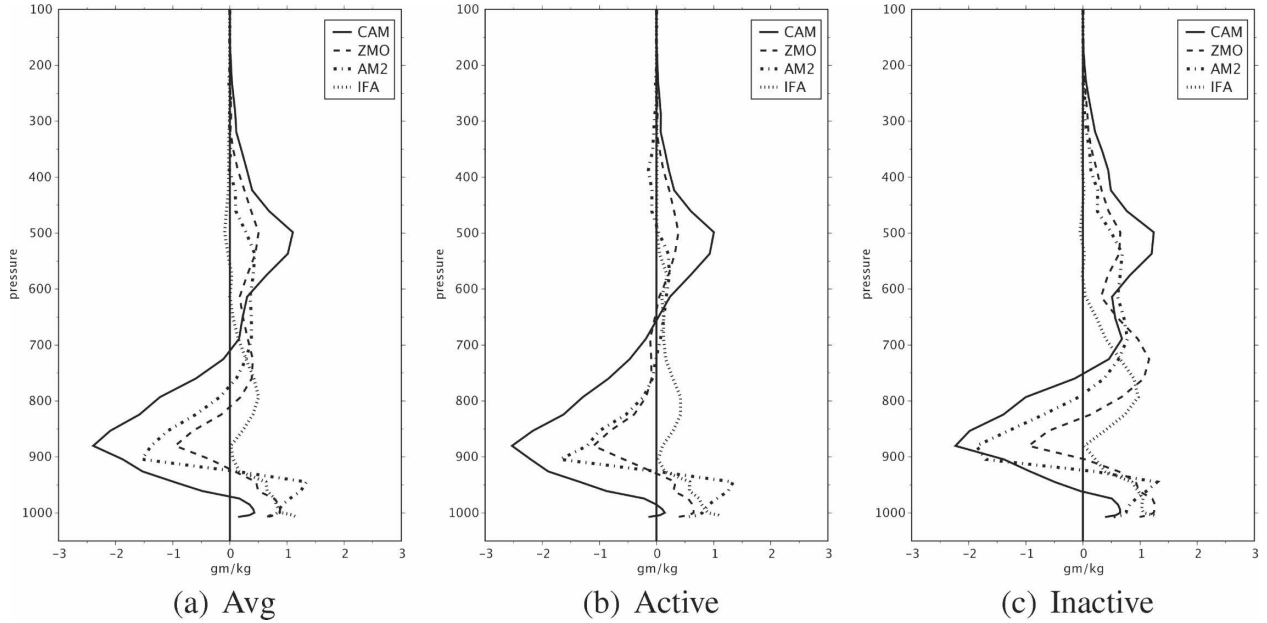


FIG. 4. Profiles of specific humidity difference ( $\text{g kg}^{-1}$ ) from the ERA-40 data for IFA observations and day-3 forecasts of CAM, ZMO, and AM2. Differences are presented for averages over the (a) entire TOGA COARE IOP, (b) active, and (c) inactive periods.

is certainly true for temperature but less so for moisture. Finally, the differing shapes of the model profiles from the IFA – ERA-40 differences indicate that the models have substantially altered the initial difference profiles, so much so as to have some confidence that the problems with the initial conditions are not dominating the answer. Finally, as the results depend on ensembles of 120 forecasts, the model differences are more likely model errors.

The specific humidity curves (Fig. 4) have a similar character across all the models. There is a tendency for the levels just below 900 hPa to be too dry and then above this level to be too wet. CAM exhibits the largest differences. For all models the differences are similar across averaging periods. Interestingly, the difference at the upper levels tends to be less for the active periods. This is at least partly due to the fact that the models' active/inactive periods do not wholly coincide with the observations. The difference profile for CAM is quite similar to that seen in climate simulations of the model in this region.

### 3) $Q_1$ AND $Q_2$ AT IFA

Some insights into the formulation of the profiles in Figs. 3 and 4 can be seen from an examination of the  $Q_1$  (apparent heat source) and  $Q_2$  (apparent moisture sink) profiles for the observations and the models averaged over the active, inactive, and entire TOGA COARE period. The equations for  $Q_1$  and  $Q_2$  are

$$Q_1/c_p = (dT/dt) + \mathbf{V} \cdot \nabla(T) + (p/p_0)^\kappa \omega(d\theta/dp) \quad \text{and} \quad (1)$$

$$Q_2/c_p = -(L_v/c_p)[dq/dt + \mathbf{V} \cdot \nabla(q) + \omega(dq/dp)], \quad (2)$$

where  $T$  is the temperature,  $q$  is specific humidity,  $p$  is the pressure,  $\omega$  is the pressure velocity ( $dp/dt$ ),  $\theta$  is the potential temperature,  $L_v$  is the latent heat of vaporization for water,  $c_p$  is the specific heat capacity of air at constant pressure,  $\kappa$  is the ratio of the ideal gas constant for dry air to the specific heat capacity of air at constant pressure, and  $p_0$  is a reference pressure (1000 hPa).

The  $Q_1$  and  $Q_2$  values for the observations are computed as residuals from temperature and moisture budgets. Thus, the  $Q_1$  includes effects of radiation and moist processes. The model values are computed to coincide as closely as possible to what the observations are attempting to estimate. Unlike the temperature and specific humidity, the  $Q_1$  profiles generally show distinct differences for the various averaging periods. As seen in Fig. 5, during the active periods the observed profiles display a heating rate maximum around the 450-hPa level. There is some indication that the heating peak occurs lower in the atmosphere for the inactive period. The CAM  $Q_1$  data (Fig. 5) has the heating maximum at a lower level and is sharply peaked. This sharp heating peak coincides with the warm bias for this model shown in Fig. 3. The rapid decrease above and below the peak compared with the observed data might

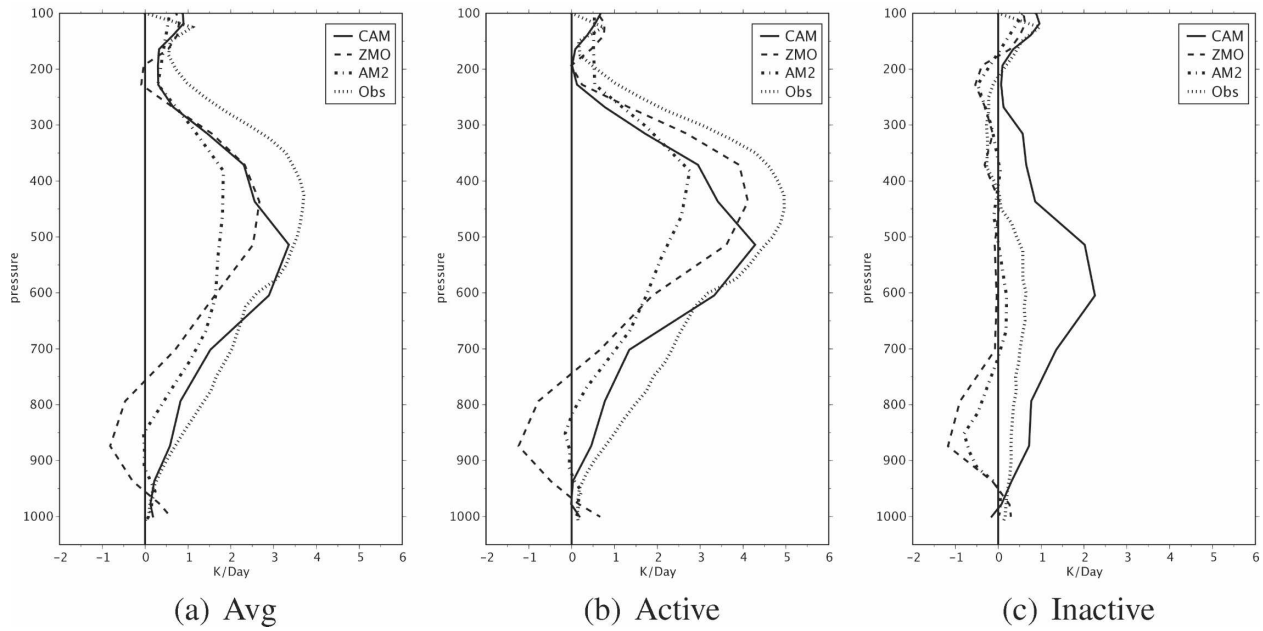


FIG. 5. Profiles of apparent heat source ( $Q_1$ ;  $\text{K day}^{-1}$ ) at the IFA for the observations, CAM, ZMO, and AM2. Averaged over (a) the entire TOGA COARE, (b) active periods, and (c) inactive periods.

contribute to the relative cooler regions in Fig. 3 on either side of the warm bias. The CAM  $Q_1$  shows significantly greater heating than the observations during the inactive periods. This is at least partially due to the fact that the periods were chosen on the basis of the observed atmosphere behavior and the CAM convective scheme is invoked when the observations indicate little activity (Fig. 2).

ZMO  $Q_1$  curves (Fig. 5) show a good agreement to the observed upper-level maximum in heating, especially during the active periods. The sharper-than-observed gradients on other side of the maximum in ZMO might contribute to the cold bias on either side of the heating maximum. The inactive  $Q_1$  for ZMO shows virtually no upper-level heating, indicating that the limiter is a bit too severe in its effects. The improvements at the upper level for the ZMO heating profile are accompanied by some anomalies at the lower levels. ZMO shows a layer of cooling for all periods below 700 mb, which is not present in the observations.

AM2 has the heating maximum at about the same level as the observations during the active periods, but the maximum has a somewhat diminished amplitude with respect to the observed data. The overall low amount of heating in the profile is consistent with the cold bias of this model. However, the shape of the curve is like that of the observed data. AM2 also shares the anomalous cooling below 700 hPa with ZMO.

Figure 6 displays a breakdown of the contributions to  $Q_1$  by various model processes. For simplicity, only av-

erages over the entire TOGA COARE experiment are shown. The relative relationships of the components are for the most part the same as the average in the active and inactive periods, the active periods having greater amplitude than the inactive.

Not surprisingly, for the tropics at this time scale, the peak of the heating due to moist processes very much determines the  $Q_1$  profiles. In both CAM versions the upper-level maximum in the moist processes is formed by an interplay of the ZM and Hack convective schemes. In both models, the ZM contribution dominates below 600 hPa and the Hack above this level. The cooling maximum at about 900 hPa in ZMO can be seen to be due to the longwave cooling, which is offset by the moist heating in CAM. The ZM heating is a factor of 2 greater in CAM compared with ZMO below 850 mb. The elevation of the  $Q_1$  peak in ZMO with respect to CAM is seen to be due to an enhanced contribution by the Hack scheme at the upper levels. The calling sequence in CAM3.1 is deep convection, shallow/middle (Hack) convection, and stratiform precipitation. Since the deep convection is called so often in CAM, it is not surprising that the Hack has so little impact since the ZM removes most of the instability. With the less frequent deep convection in ZMO, Hack convection is more active. The mediating or fill-in role played by the Hack scheme does make the comparison of the two deep convective routines a bit more problematic. Zhang and Mu (2005) found in extended climate simulations that the relative behavior of the deep

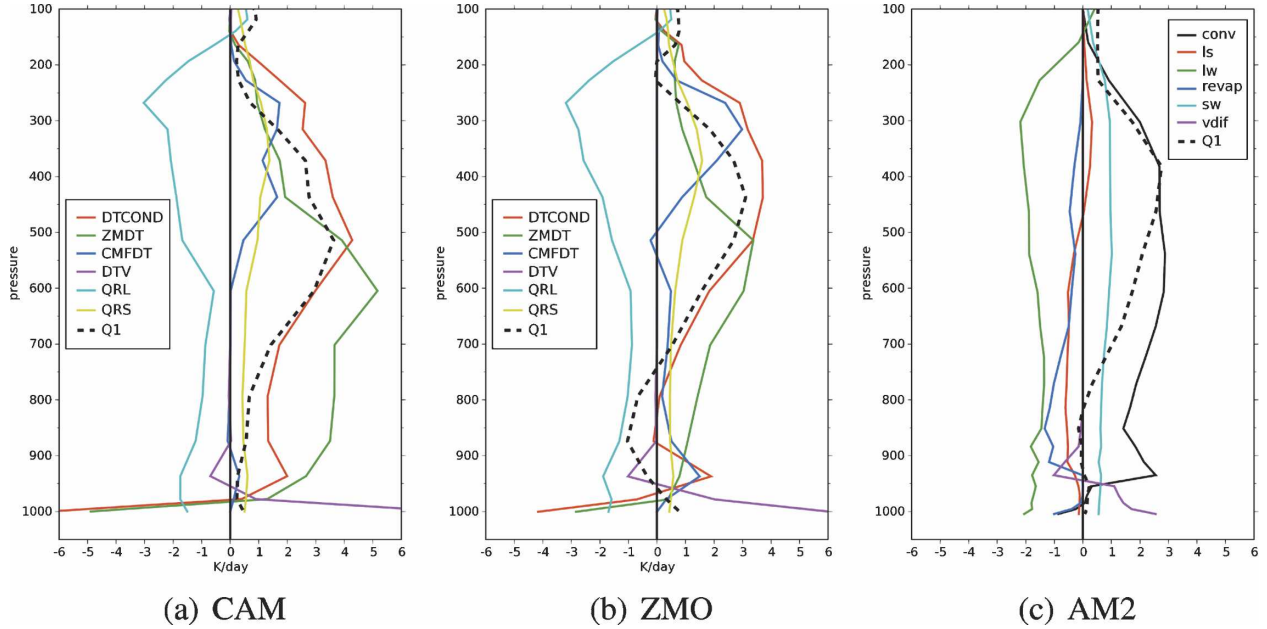


FIG. 6. Profiles of the components making up the apparent heat source ( $Q_1$ ;  $K \text{ day}^{-1}$ ) at the IFA for the (a) CAM, (b) ZMO, and (c) AM2. DTCOND: moist processes, ZMDT: deep convection, CMFDT: Hack (shallow) convection, DTV: vertical diffusion, QRL: longwave radiation, QRS: shortwave radiation, conv: convective, sw: shortwave radiation, lw: longwave radiation, revap: reevaporation of precipitation, ls: large-scale precipitation, and vdiff: vertical diffusion. Note that for CAM, DTCOND includes both ZMDT and CMFDT plus some other processes not broken out. Here  $Q_1(\text{CAM}) = \text{DTCOND} + \text{DTV} + \text{QRL} + \text{QRS}$ , and  $Q_1(\text{AM2}) = \text{conv} + \text{sw} + \text{lw} + \text{ls} + \text{vdiff}$ .

convection and the Hack scheme in CAM and ZMO was quite similar to that seen here. They pointed out that the Hack and ZMO convection play realistic roles with respect to the MJO. The Hack scheme can be active at times when the moisture structure is not conducive to deep convection, and the Hack modification of the environment can enhance the impact of the deep schemes. The lack of the Hack contribution in the CAM is viewed as a deviation from observed MJO behavior by Zhang and Mu (2005).

Two additional experiments were run to attempt to better isolate the effects of the Hack convection. CAM and ZMO were integrated with the Hack scheme turned off (NoHack). All other aspects of the models remained the same. The NoHack precipitation time series were quite similar to Fig. 2 for CAM and ZMO. The heating profiles for the deep convection for the NoHack runs were much like those in Fig. 6. The basic character of the deep convective schemes was unaltered by the elimination of the Hack parameterization and since the deep convection dominates the rainfall, the precipitation time series is similar between the two runs. In the NoHack simulations the large-scale precipitation, which was small in the CAM and ZMO simulations, plays a larger role. With regards to sign, the large-scale heating profiles were much like the large-scale

component in AM2 (Fig. 5). It is positive above 500 hPa and negative below. In the CAM and ZMO NoHack simulations the upper-level heating is about 2 times larger than in AM2. In the NoHack simulations, the large-scale upper-level heating raises the heating peak to be more top heavy and more in line with the observations. The heating profiles for large-scale heating for both NoHack simulations are consistent with the observational estimates of heating by stratiform precipitation by Lin et al. (2006). At least for this particular experiment, there are indications that turning off the Hack scheme might improve some aspects of CAM.

The  $Q_1$  profiles for AM2 are shown in Fig. 5. For the active periods the AM2  $Q_1$  resembles that of ZMO although the amplitude of the upper-level heating is much smaller in AM2. Both have a similar low-level cooling below 750 hPa, at odds with the observations. The average  $Q_1$  for AM2 does not have the well-defined peak of the observations, but rather a slight local maximum at 400 hPa. Examining the components of  $Q_1$  in AM2 (Fig. 6), it can be seen that the heating maximum for AM2 is due to the interplay of the large-scale and convective heating. On average the large scale has a relatively smaller amplitude, and this results in the modest maximum at the upper levels.

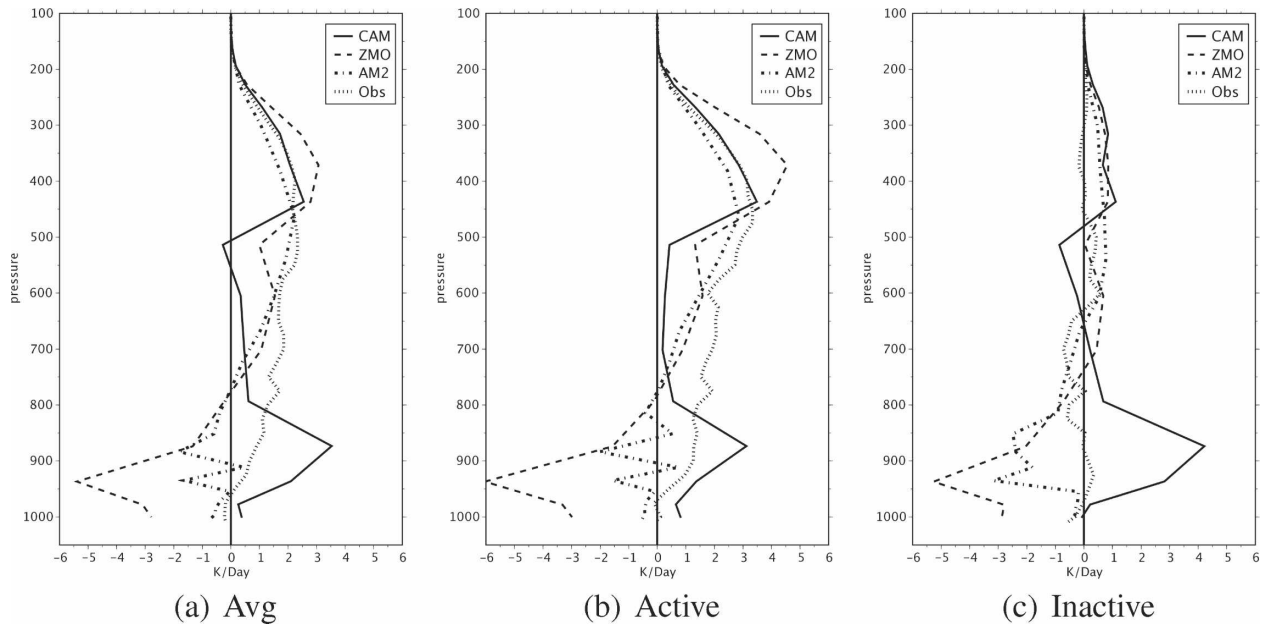


FIG. 7. Profiles of the apparent moisture sink ( $Q_2$ ;  $\text{K day}^{-1}$ ) at the IFA for the observations, CAM, ZMO, and AM2. Averaged over (a) the entire TOGA COARE, (b) active periods, and (c) inactive periods.

Two additional experiments were run to attempt to better isolate the effects of the Hack convection. Both CAM and ZMO were integrated with the Hack scheme turned off (NoHack). All other aspects of the models remained the same. The NoHack precipitation time series were quite similar to Fig. 2 for CAM and ZMO. The heating profiles for the deep convection for the NoHack runs were much like those in Fig. 6. The basic character of the deep convective schemes was unaltered by the elimination of the Hack parameterization and since the deep convection dominates the rainfall, the precipitation time series was similar between the two runs. In the NoHack simulations the large-scale precipitation, which was small in the CAM and ZMO simulations, plays a larger role. With regards to sign, the large-scale heating profiles were much like the large-scale component in AM2 (Fig. 5). It is positive above 500 hPa and negative below. In the CAM and ZMO NoHack simulations the upper-level heating is about 2 times larger than in AM2. In the NoHack simulations the large-scale upper-level heating raises the heating peak to be more top heavy and more in line with the observations. The heating profiles for large-scale heating for both NoHack simulations are consistent with the observational estimates of heating by stratiform precipitation during MJO events by Lin et al. (2006). At least for this particular experiment, there are indications that turning off the Hack scheme might improve some aspects of the CAM simulations.

Figure 7 is the observed apparent moisture sink ( $Q_2$ )

averaged over the same periods as the  $Q_1$  data. Ciesielski et al. (2003) compute the impacts that the moisture corrections have on the estimates of  $Q_2$  for the IOP. The change is positive at all levels and decreases with height. The change has a maximum at the surface of about  $0.75 \text{ K day}^{-1}$ , decreasing to  $0.5 \text{ K day}^{-1}$  at 900 hPa and further decreasing to near zero at 700 hPa. Given the magnitudes of the differences in Fig. 7, it is probably safe to assume that the ERA-40-IFA data differences will not be a determining factor on the interpretation of the results.

The observed mean values (Fig. 7) evince a drying throughout the column with a slight maximum at about 450 hPa for the active periods. The magnitude of the drying is fairly constant between 800 and 400 hPa. Both CAM models show more structure than the observed data with distinct extrema at the upper and lower levels.

Both CAM versions have a drying peak at about 400 hPa, but the ZMO peak is broader and at a higher level than that of CAM. CAM has a drying peak at 900 hPa, which has an amplitude comparable to the upper-level feature. This is a factor of 4 greater than observations, and could account for the CAM lower-level dry bias. ZMO has a moistening maximum at about 950 hPa, in sharp disagreement with CAM and observations. This moistening would help explain the reduction of the dry bias seen in CAM but at the price of introducing behavior apparently at odds with observations. The large bias of ZMO in  $Q_2$  at the lower levels is largely offset by advection (not shown), resulting in the modestly biased

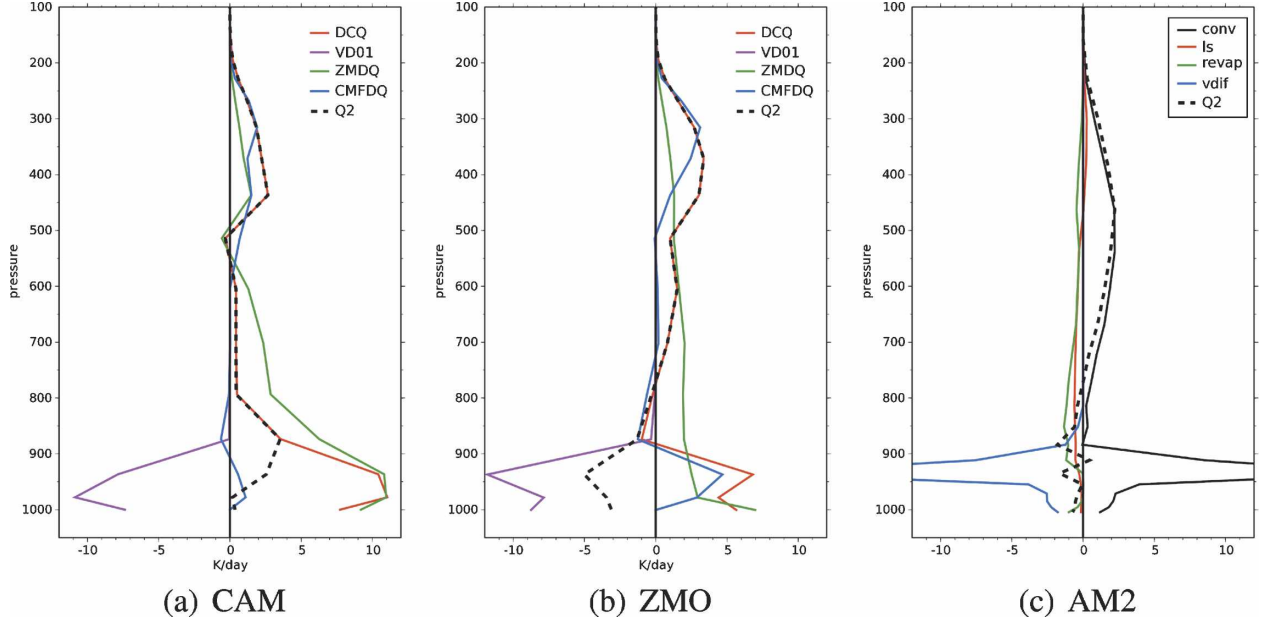


FIG. 8. Profiles of the components making up the apparent moisture sink ( $Q_2$ ;  $K \text{ day}^{-1}$ ) at the IFA for (a) CAM, (b) ZMO, and (c) AM2. DCQ: moist processes, VD01: vertical diffusion, ZMDQ: Zhang–McFarlane deep convection, CMFDQ: Hack shallow convection, conv: deep convection, ls: large-scale precipitation, revap: reevaporation of precipitation, and vdiff: vertical diffusion. Note for CAM, DCQ includes both ZMDQ and CMFDQ plus some other processes not broken out. Here  $Q_2(\text{CAM}) = \text{DCQ} + \text{VD01}$ , and  $Q_2(\text{AM2}) = \text{conv} + \text{ls} + \text{vdiff}$ .

specific humidity (Fig. 4). AM2 at the upper levels (i.e., above 600 hPa) compares fairly well with the observed  $Q_2$ . The AM2 maximum of drying is about  $2 \text{ g kg}^{-1} \text{ day}^{-1}$  while the observations have a value of  $3.5 \text{ g kg}^{-1} \text{ day}^{-1}$ . AM2 is noisy below 850 hPa, but there is a tendency toward a bit more moistening than seen in the observations.

Figure 8 presents the profiles of the main components making up the  $Q_2$  for the models. The much reduced role of drying by the deep convection in going from CAM to ZMO accounts for the anomalous low-level moistening in ZMO. As in the  $Q_1$  plots, the Hack scheme plays a more prominent role in ZMO as compared with CAM. In the lower levels the strong moistening is at odds with the observations. As with the  $Q_1$  profiles, the AM2 and ZMO  $Q_2$  profiles have a similar shape, AM2 having a reduced amplitude with respect to ZMO. In AM2 the small low-level moistening appears to be a small imbalance between very large contributions from the convective drying and vertical diffusion moistening.

#### 4) ZONAL WIND AT IFA

Figure 9 displays the profiles of the time-average zonal wind at the IFA for the observations and the day-3 forecasts of CAM, ZMO, and AM2. The ERA-40 zonal wind (not shown) agrees well with the IFA data.

CAM and observations show fair agreement except for the sharp decrease in amplitude in CAM below 850 hPa. The model tends to underestimate the zonal wind in the lowest levels. The model slightly overestimates the westerly wind above 800 hPa. ZMO has a similar behavior for this variable but with a bit more easterly bias at the lowest levels. The 26-level CAM has rather coarse resolution at the lowest levels. An experiment with a 30-level version of CAM was run to ascertain whether the poor low-level resolution might account for the bias in the zonal wind simulation. The 30-level CAM used here has 8 levels below 800 hPa, as compared with 4 in the 26-level CAM. The 30-level model winds (not shown) present some small differences in structure attributable to the finer resolution of the model, but the increased resolution produces essentially the same profile as in Fig. 9.

Figure 10 displays the time series of the zonal wind at 900 hPa for the observations and the day-3 CAM forecasts at the IFA. This figure clearly shows the strong easterly bias of the model, which is especially evident during periods of stronger observed westerlies. This underestimation of the westerly zonal wind can also be seen in climate simulations of CAM in the IFA region. The climate December–February (DJF) values of the lowest-level zonal wind in CAM display an underestimate of  $2\text{--}3 \text{ m s}^{-1}$  over the TOGA COARE region

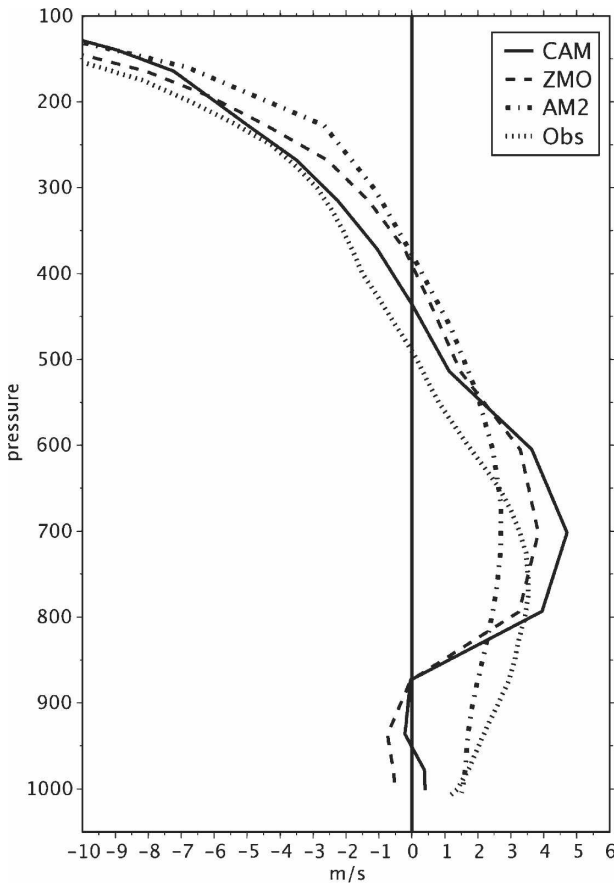


FIG. 9. Profile of average zonal wind ( $\text{m s}^{-1}$ ) at the IFA for the observations and day 3 of CAM, ZMO, and AM2.

compared with the National Centers for Environmental Prediction (NCEP) reanalysis.

Figure 10 shows that AM2 produces a very credible simulation of the zonal wind at this level without the significant problems exhibited by both versions of CAM used here. AM2 has more model layers (i.e., 9) in the boundary layer than CAM (i.e., 4). However, the 30-level CAM experiment indicates that the number of levels in the boundary layer is not a sufficient condition to ensure a good simulation. AM2 does have a representation of momentum transport by convective processes, which CAM does not. AM2 has a mechanism for relating momentum transport to the cumulus mass flux predicted by the relaxed Arakawa–Schubert (RAS) convective scheme (GFDL Global Atmospheric Model Development Team 2004). The vertical gradient of the zonal wind is strongly positive in AM2 during the wind burst events. Given this gradient the CMT scheme of AM2 will contribute to an increase in the zonal wind at 900 hPa.

The forcing of the wind during MJO events is rather complex. The wind is a result of the interplay of the

large-scale pressure gradient, mesoscale- and cumulus-scale momentum fluxes, and pressure gradients. It is the latter two forcings that the climate models attempt to parameterize. As the subsequent very brief discussion attempts to point out, it is still uncertain as how to best capture these forcings in a climate simulation. Gutzler et al. (1994) remark that the TOGA COARE IOP has anomalously strong westerly flow over the IFA and relate this observation to the MJO passages. Lin et al. (2005) indicate by a residual technique the importance of subgrid-scale processes in decelerating the zonal flow during an MJO passage. Houze et al. (2000) show that mesoscale circulations act to slow down the westerly wind in the onset region of the MJO and transport westerly momentum downward in the strong westerly region, thus accelerating the lower-level wind burst after onset. Mechem et al. (2006), using a cloud resolving model, indicate that the convective and stratiform regions are both important in describing the momentum transport for the TOGA COARE MJO passages. They show that sometimes these subgrid-scale mechanisms work in concert and sometimes oppose the sense of the large-scale momentum transport. Furthermore, the convective and stratiform fluxes can have different roles depending on the phase of the MJO. Such complications make the parameterization of the momentum budget quite problematical during these events. Indeed, it was in part because of these uncertainties that AM2 used the simpler [simpler than mass flux formulations; e.g., Gregory et al. (1997)] diffusive scheme.

Experiments were run using a version of CAM3.1 modified as described by Wu et al. (2003). This version of the model includes a parameterization of cumulus momentum transport and a modified deep convection similar to the modified ZM used here. The Wu et al. (2003) CMT is a mass flux formulation taking into account the momentum transported by the inferred cloud mass flux and also momentum changes forced by the convection-induced pressure gradient force. The results for the zonal wind were very similar to CAM. The simulation with CMT exhibited a wind profile very close to that of CAM and ZMO in Fig. 9 and also underestimated the zonal wind, similar to ZMO in Fig. 10. These results indicate a noncritical role at least for this particular parameterization at this location. The GFDL Global Atmospheric Model Development Team (2004) comments that the diffusive coefficients for the AM2 CMT are larger at low levels than an equivalent mass flux formulation. The AM2 results would give some evidence that perhaps the simpler diffusive scheme is superior in this very complex situation. It should be noted that no experiments were conducted

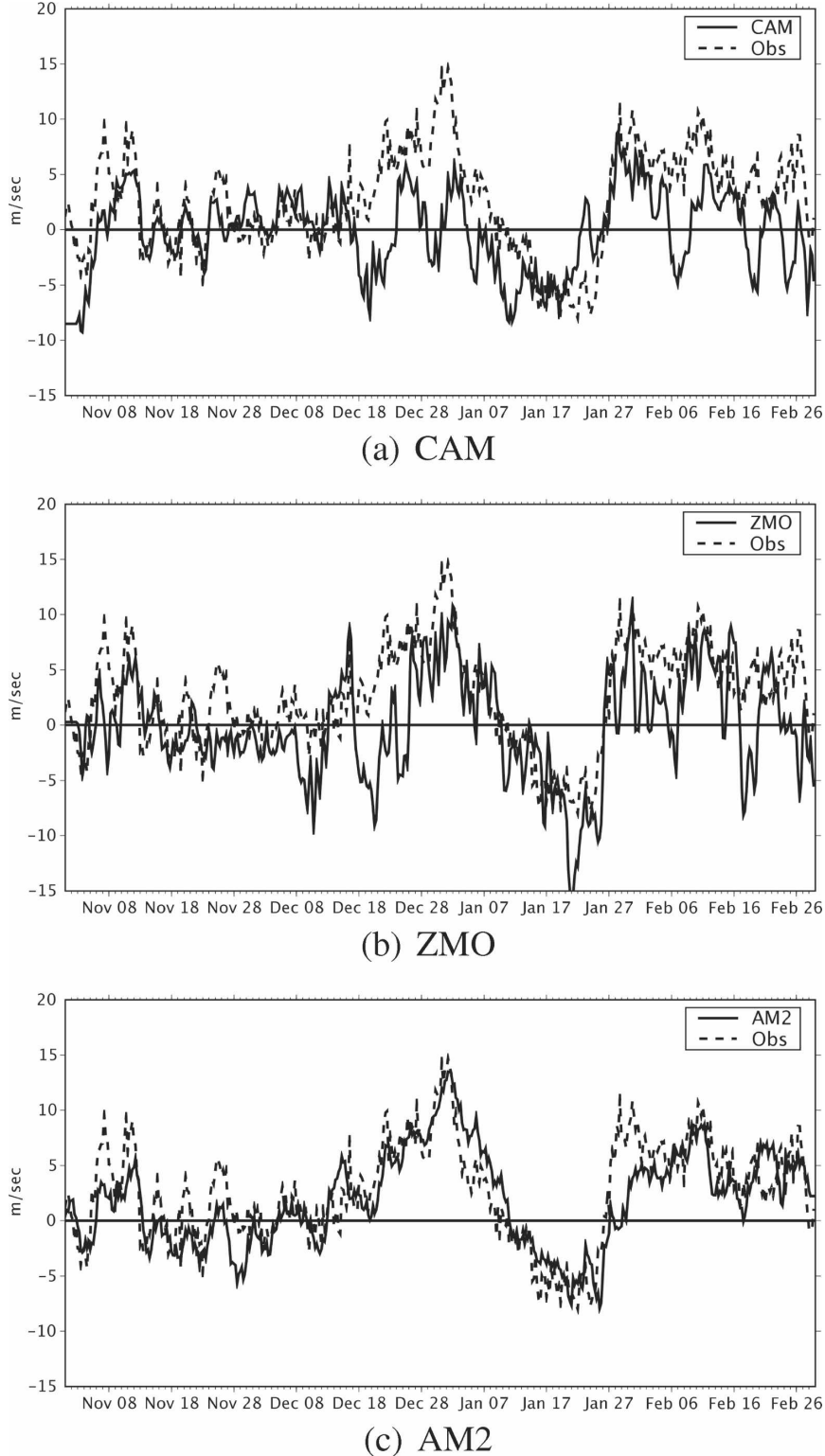


FIG. 10. Zonal wind at 900 hPa ( $\text{m s}^{-1}$ ) for the TOGA COARE IFA. Observational estimate from IFA array budget and (a) CAM forecast day 3, (b) ZMO forecast day 3, and (c) AM2 forecast day 3.

turning off CMT in AM2, so there is no definitive proof that this parameterization played a major role in AM2's wind simulation.

### *b. Equatorial tropics*

#### 1) 200-hPa VELOCITY POTENTIAL

A very commonly used diagnostic to monitor MJO activity is a longitude–time plot of bandpassed-filtered 200-hPa velocity potential. Figure 11 displays the time–longitude plots of the bandpass (30–70 days) 200-hPa velocity potential for the ERA-40 and days 3 and 6 of the CAM, ZMO, and AM2 simulations averaged from 5°S to 5°N. The bandpass filter is a second-order tangent Butterworth filter, applied in the frequency domain (Otnes and Enochson 1978). This analysis provides a useful overview of the ability of the models to capture and maintain the intraseasonal variability present in the upper-tropospheric circulation. The ERA-40 data (top panel, Fig. 11) shows the two MJO events that passed through the central TOGA COARE array (2°S, 155°E) during the experiment. The sign convention of the figure is such that local minima correspond to active (upper-level divergence) regions. The good correspondence between the top panel of Fig. 11 with Fig. 1 increases confidence in both fields.

Figure 11 demonstrates the ability of all the models to maintain the basic MJO feature for 3 days. Both AM2 and ZMO maintain a fair representation out to 6 days, but CAM shows a drastic falloff in amplitude. Comparison of the ERA-40 data and CAM in Fig. 11 indicates that even at day 3 CAM had begun to diminish significantly. Zhang and Mu (2005) demonstrate that this ZMO can produce realistic MJO variability in coupled model climate simulations although it appears to overestimate the amplitude in Fig. 11. Some possible reasons for this behavior will be put forth in a later section. Keep in mind that the models are initialized by the ERA-40 state at the start of each forecast. Thus, the possible diminution of the MJO in CAM is consistent in all phases and locations of the oscillation. Agudelo et al. (2006) performed 30-day forecasts using the ECMWF climate model for the TOGA COARE period. Agudelo et al. (2006) noted that the forecasts started before the transition period, that is, the period between the suppressed and active phases of the MJO, did a poor job in simulating the convective activity. The short-term forecasts reported here indicate that CAM systematically underestimates the MJO amplitude during all the phases of the oscillation. The decrease in amplitude at 6 days is more than can be attributed to the fact that the model does not have an interactive ocean (Rajendran and Kitoh 2006).

#### 2) RAINFALL AND 850-hPa WIND

Figure 12 presents time–longitude plots of pentad rainfall data from the Climate Prediction Center (CPC) Merged Analysis of Precipitation (CMAP) and SSM/I observations and ERA-40 850-hPa zonal wind averaged from 5°S to 5°N. The two rainfall datasets agree rather well on the location (in space and time) of the rain events, but the SSM/I events consistently have somewhat more amplitude. The westerly wind burst associated with the first MJO is prominent as the MJO approaches the date line at about 28 December. The phasing and relative locations of the wind and rain maxima are in close agreement with the careful analysis of Lin and Johnson (1996). The maximum in the rainfall precedes the westerly wind peak, the maximum winds occurring just as the active period rain passes. The second MJO that reaches the date line at the end of January has some indications of this wind and rain structure, but it is not as well delineated as the first. Lin and Johnson (1996) only use the first MJO as an archetypical model. For the first MJO the IFA is to the west of the most intense rain and strongest wind bursts.

Figure 13 is the same as Fig. 12, except that it shows the model rain and winds for day 3 of the forecast. CAM does capture the pattern of the rainfall but it is evident that the model's underestimate of intensity is not confined to the IFA. The precipitation events of ZMO appear to be too intense compared with CMAP but are more in line with SSM/I. However, these short-lived intense precipitation events in ZMO do not evince the eastward progression seen in the observations. ZMO does have an increase in precipitation activity in the Indian Ocean with respect to CAM, which is a significant improvement since Waliser et al. (2003) cite the lack of precipitation activity in the Indian Ocean as being common to many AGCMs.

The plot of AM2 in Fig. 13 indicates that the model is more active than CAM but less than the observations. The pattern of the rain with respect to the westerly wind burst at the end of December is in fairly good agreement with the observations, albeit the amplitudes of the rain and wind are too small. Although AM2 underestimates the wind burst just west of the date line, its westward extension is such that at the location of the IFA a good simulation is achieved (Fig. 10).

The pattern correlations between the rain CMAP observations and CAM forecasts decrease from 0.7 at day 3 to 0.59 at day 6 (not shown). The average rainfall over the figure remains at  $4.6 \text{ mm day}^{-1}$  for days 3 and 6 compared with an observed value of 4.98. ZMO has a larger rainfall amount than CAM and the averages for days 3 and 6 are 5.3 and 5.6, respectively. The increased

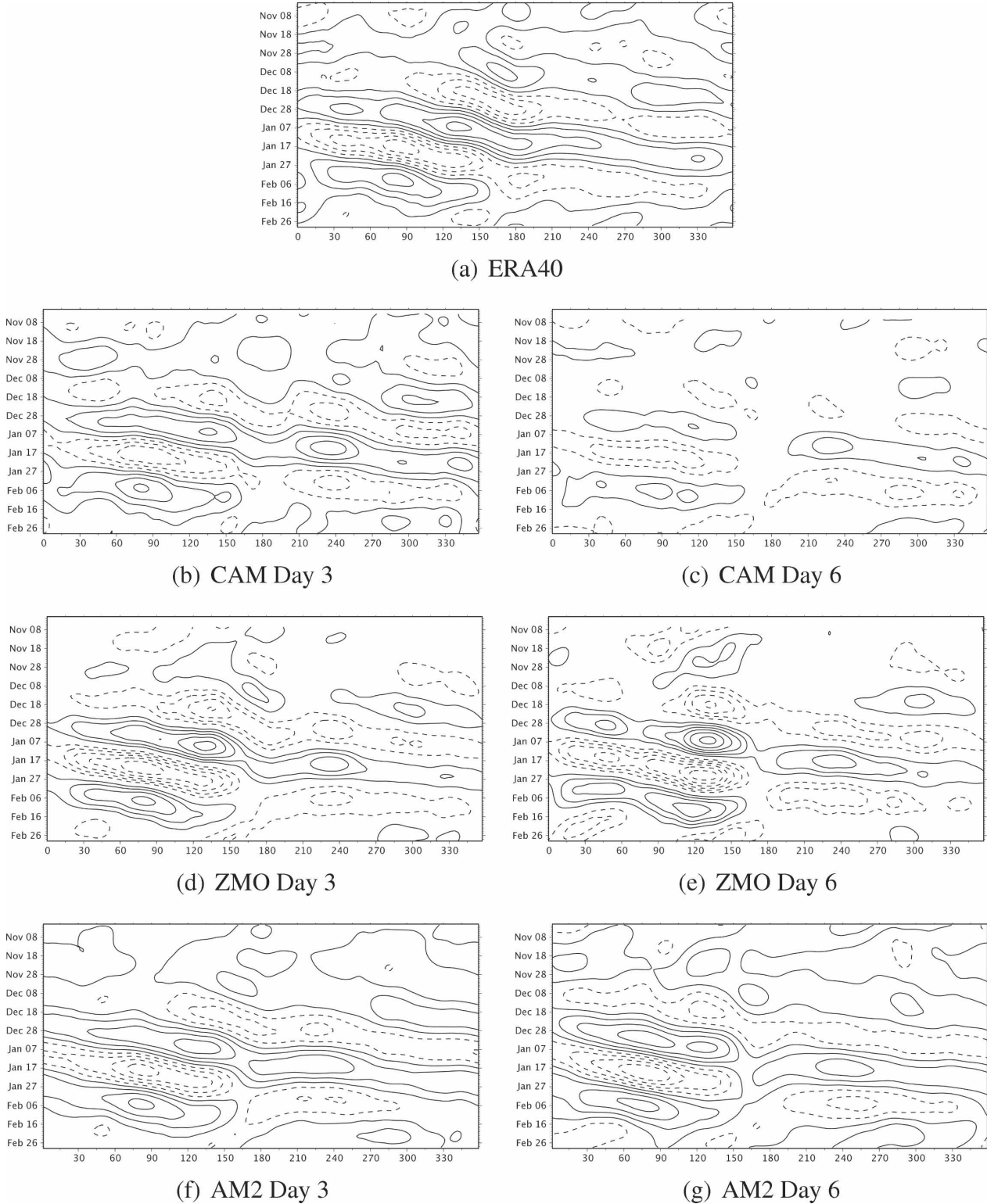


FIG. 11. Velocity potential, bandpass-filtered 30–70 days, averaged from 5°S to 5°N. Shown are the ERA-40 observations and days 3 and 6 of the CM, ZMO, and AM2. The contour interval is  $2 \times 10^6 \text{ m}^2 \text{ s}^{-1}$ . Negative contours are dashed.

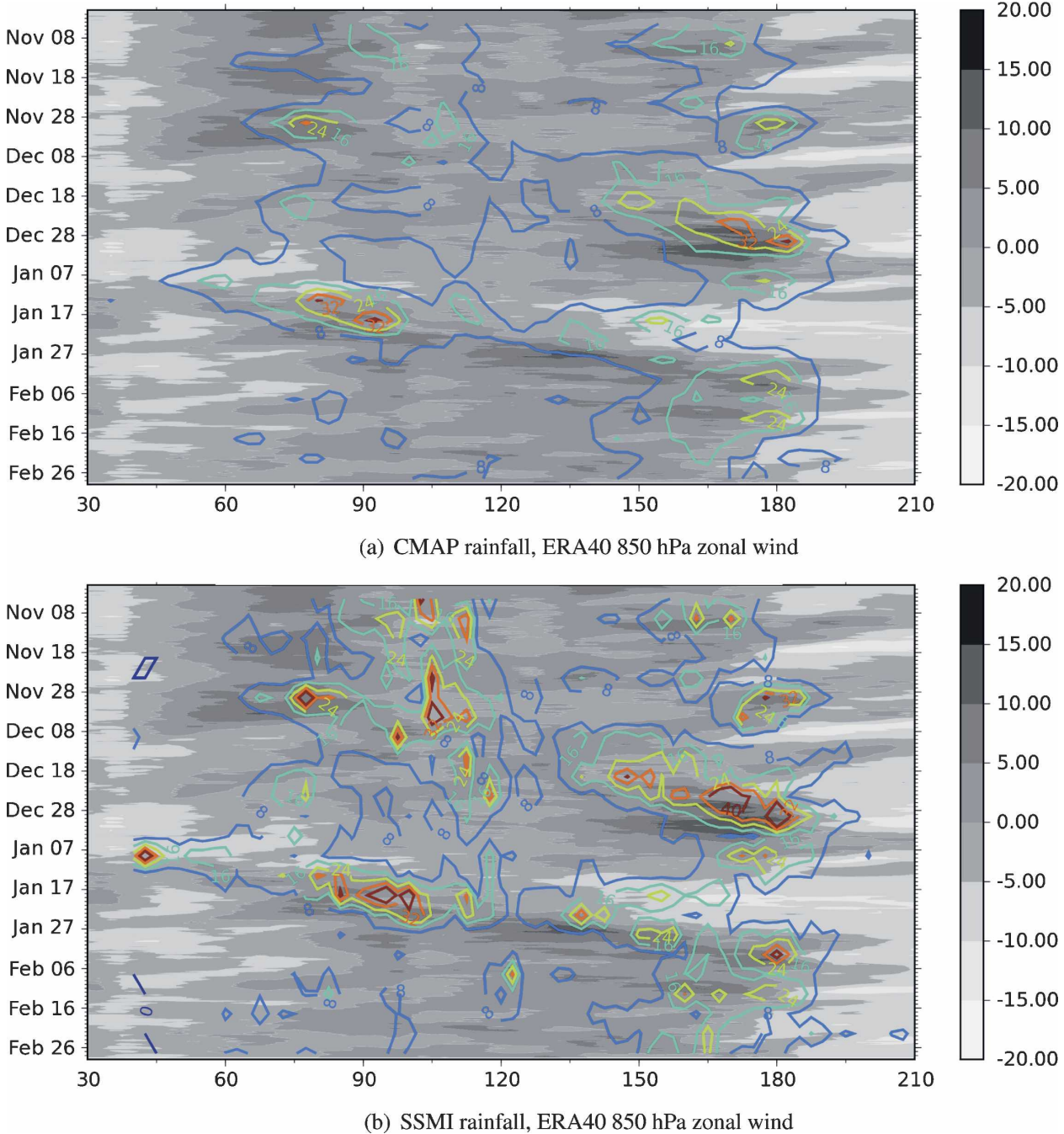


FIG. 12. Contours of (top) CMAP and (bottom) SSM/I rainfall ( $\text{mm h}^{-1}$ ) and shading of ERA-40 zonal wind ( $\text{m s}^{-1}$ ) at 850 hPa. The SSM/I data have been put on the pentad times. Contours for rain are in units of  $8 \text{ mm h}^{-1}$ .

activity in ZMO does not capture the observed variation too well; the pattern correlation for day 3 is 0.5 and this decreases to 0.48 by day 6. The pattern correlation of the AM2 rainfall with CMAP falls from 0.7 on day 3 to 0.64 on day 5.

In an attempt to get at some possible causes of the differences seen in Fig. 13, simulations were run for a

different set of variations on CAM. The models used are 1) ZMO with the RH limiter criterion set to zero, 2) CAM using the modifications of Wu et al. (2003), which is very similar to the ZMO deep convection parameterization but with a complex cumulus momentum transport added, and 3) CAM with 30 vertical levels. The elimination of the RH limiter in ZMO has a dramatic

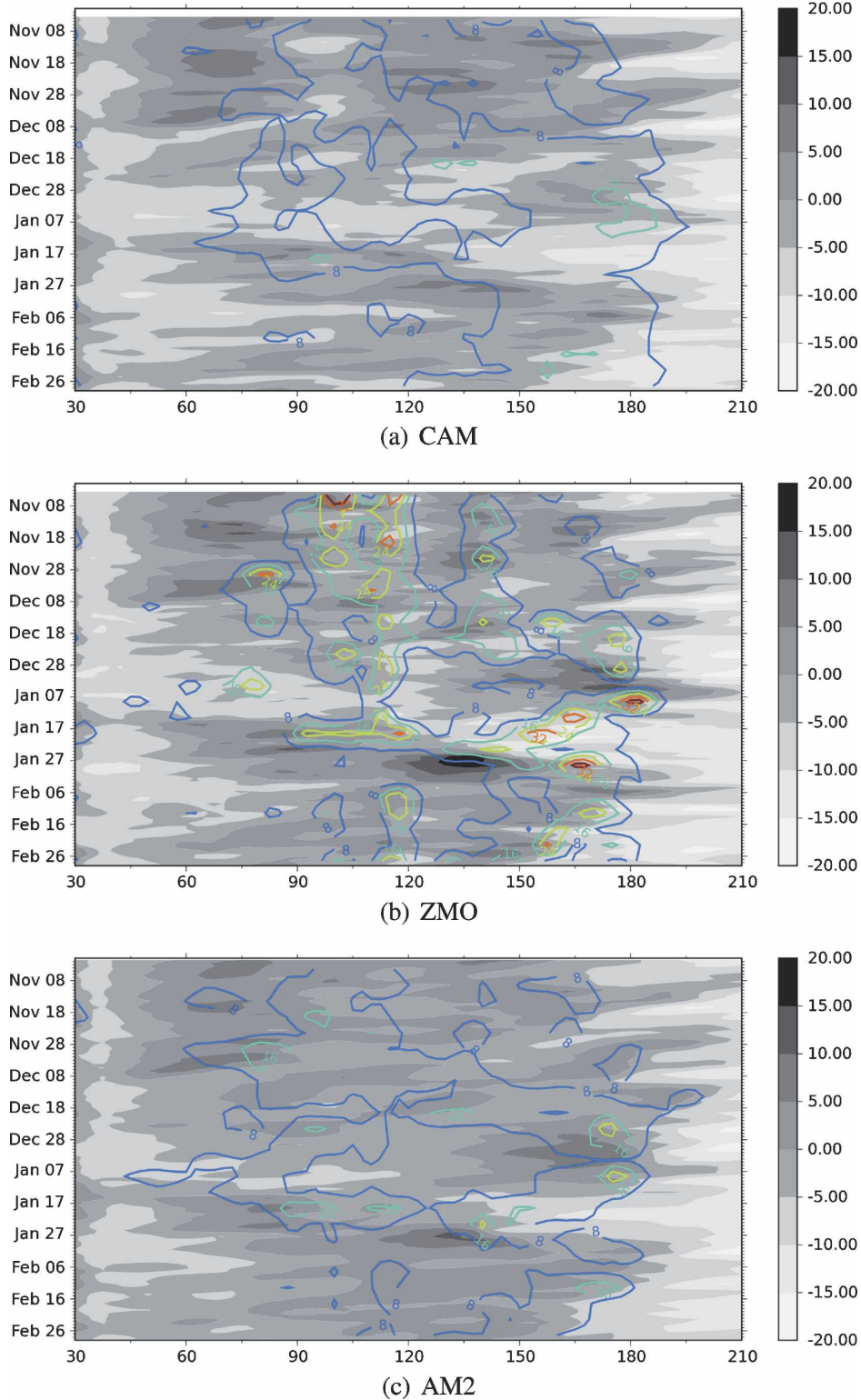


FIG. 13. Contours of rainfall ( $\text{mm h}^{-1}$ ) and shading of zonal wind ( $\text{m s}^{-1}$ ) at 850 hPa for the (top) CAM, (middle) ZMO, and (bottom) AM2 day-3 forecasts. Contours for rain are in units of  $8 \text{ mm h}^{-1}$ .

impact on the character of the rainfall. While the rainfall has more intensity than in CAM, it is diminished considerably compared with ZMO. The Wu et al. (2003) scheme produces an 850-hPa wind simulation (not shown) very similar to that of ZMO. This would indicate a negligible role for the CMT parameterization in this model for this set of integrations. The poor extension of the westerly wind maxima to the west is similar to that of ZMO so that the wind at the IFA has an underestimate of the bursts, much like in ZMO. A critical aspect of capturing the wind burst would appear to be the systematic intensification of the rain as the disturbance moves eastward, which is not handled well by either model. CAM with 30 levels is seen to behave in a very similar fashion to the 26-level model.

### 3) REGIONAL RAIN AND 850-HPa WIND

The preceding sections provided a complete view in time with respect to the models' tropical performance but sacrificed spatial detail to achieve this completeness. In this section latitude-longitude plots will be presented to give a two-dimensional perspective to the rain and low-level wind field for specific time periods. An obvious candidate for such an examination is the MJO passage at the IFA in mid-December.

Figure 14 presents the rainfall averaged over days preceding and after the passage of the first MJO at the IFA. The CMAP rainfall is used, but the SSM/I data showed the same character. The observations show the expected shift and strong intensification of rain from the west of the IFA to the east. Inspection indicates that AM2 captures the eastward progression with the most fidelity of all the models. Keep in mind that the models do not forecast a large propagation in the 2-day forecast. Rather, this is a demonstration of how the models respond to the varying dynamics presented to them as the MJO proceeds eastward. Note that this also shows that AM2 is capable of greater rainfall intensity than CAM, which is not obvious from the IFA time series. CAM shows almost no difference in the two plots. ZMO also shows a good correspondence to the observations, except it overestimates the rain in the region of New Guinea in both time periods. This overestimate of rain over New Guinea and its environs is endemic to ZMO and is quite apparent in the tropical error pattern for the entire TOGA COARE period shown later in this section.

Figure 15 displays the 850-hPa wind, mean sea level pressure (MSLP) for the ERA-40, and the difference from these values for the models for the period 11 December–1 January. This encompassed the period of the westerly wind maxima seen in Fig. 10. CAM shows the largest differences with a large underestimate of the

east–west pressure gradient along the equator. The very weak rainfall response seen in Fig. 14 is consistent with the dynamics' failure to establish the needed pressure gradient. The quality of ZMO is affected by the anomalously strong rainfall over and to the south of New Guinea. This sets up the anomalous circulation to the west of the IFA, which disrupts the westerlies and sets up some northerly flow over the IFA. AM2 has the smallest wind error, in agreement with Fig. 10 at the IFA. This is consistent with this model's good representation of the observed rain pattern.

Looking over all the wind maxima and rainfall relationship in Fig. 12, it appears that the eastward intensification of rainfall is often followed by an increase in the westerly wind. The ZMO progression of rain is in fits and starts, disrupting the establishment of the winds. CAM has such small intensity as to be wholly ineffective. While having a reduced intensity with respect to the observations, AM2 does capture the rain progression smoothly and produces a weaker wind maximum but is well positioned.

The evaluation of the lower-level zonal wind in the models presents a challenge. Figure 9 indicates clearly that on average CAM and ZMO underestimate the strength of the zonal wind below 800 hPa, while AM2 performs better. Figure 10 illustrates that at the IFA, the manner in which CAM and ZMO achieve the average values is quite different. In Fig. 10, ZMO is seen to be better than CAM during the peak westerly winds in late December but has other discrepancies such that the mean is not that different in Fig. 9. It is seen in Fig. 15 that beyond the IFA, ZMO displays much less widespread bias than CAM for the period considered. Note that some of the largest wind differences in Fig. 15 for ZMO occur over the IFA. Just using the evidence from Fig. 9 it would seem that CAM and ZMO share the same zonal wind properties, but extending in time beyond the average and in space beyond the IFA, ZMO appears to have a distinct advantage over CAM. AM2 consistently has the best simulation for all these aspects of the zonal wind.

## 6. Discussion

The work here indicates that given realistic initial states, CAM deviates from the observations rather quickly. This result demonstrates that the representation of shorter-term processes and likely convection is at fault in this model. The modification of the ZM scheme increased the activity of the model but at the expense of generating some problematic heating profiles. The new scheme does increase the intensity of precipitation events but these events do not have a high correlation to observations. The correlation for the

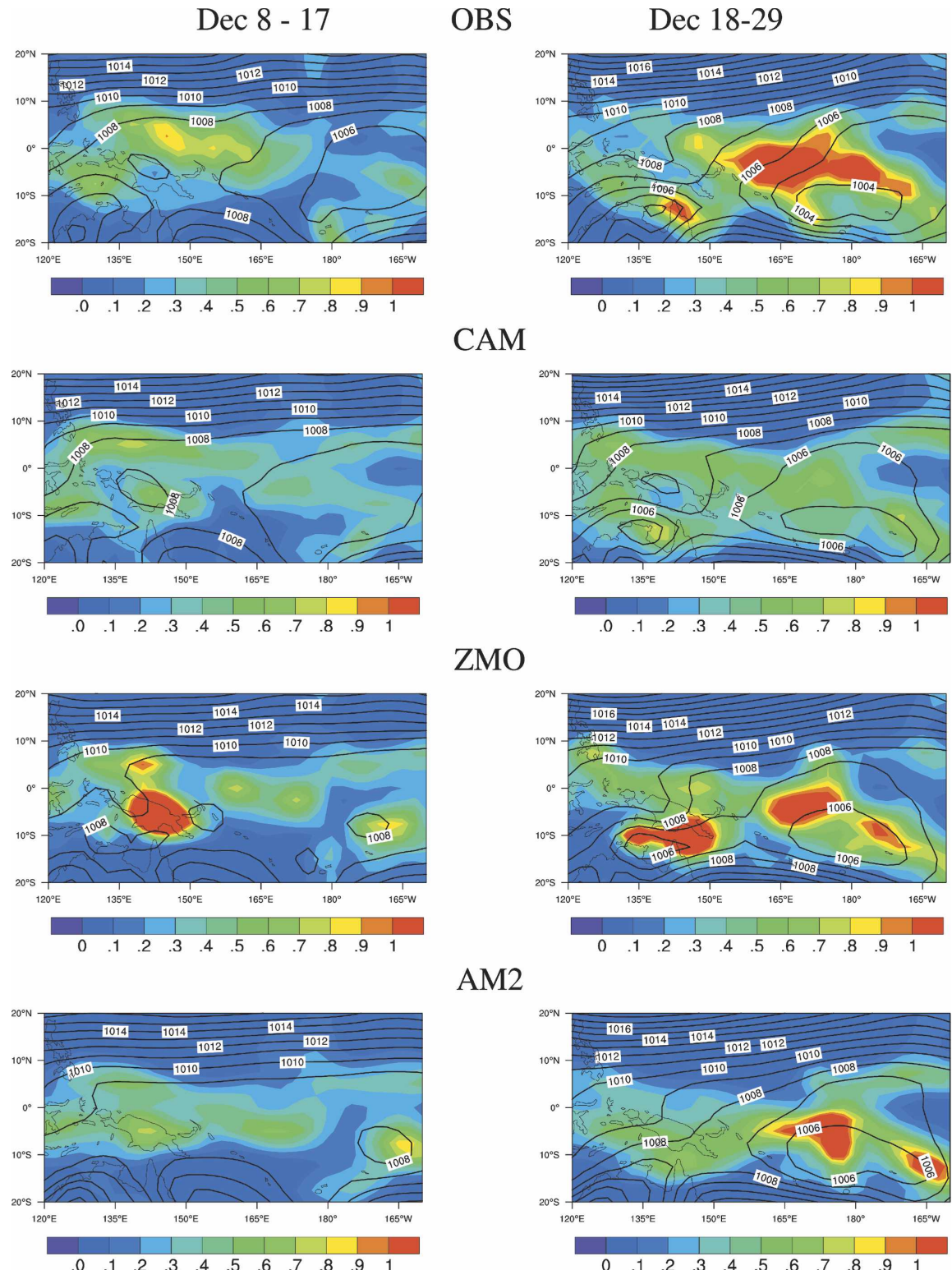


FIG. 14. Rainfall ( $\text{mm day}^{-1}$ ) and MSLP (mb) for the period (left) 8–18 Dec and (right) 18–29 Dec. (top to bottom) Observational CMAP estimate, CAM forecast day 3, ZMO forecast day 3, and AM2 forecast day 3.

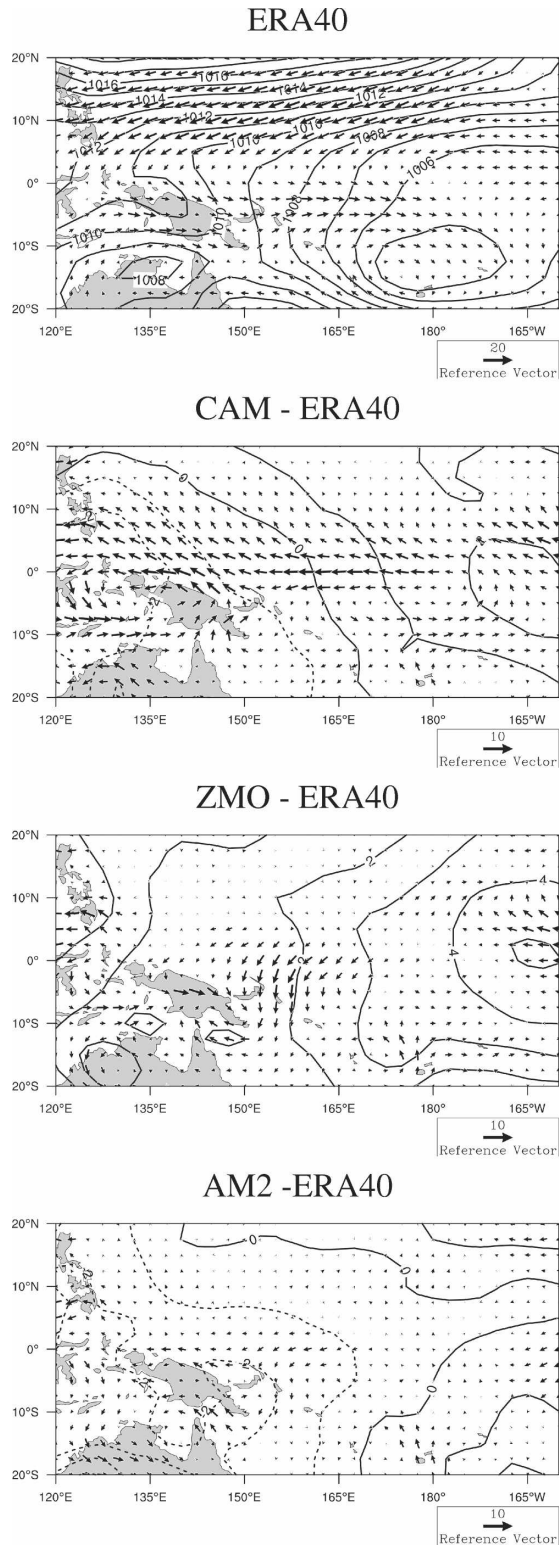


FIG. 15. 850-hPa winds ( $\text{m s}^{-1}$ ) and MSLP (mb) for the period 11 Dec–10 Jan. (top to bottom) Observed ERA-40, difference between CAM forecast day 3 and ERA-40, difference between ZMO forecast day 3 and ERA-40, and difference between AM2 forecast day 3 and ERA-40.

data in Fig. 13 drops to 0.5 by day 3 of the forecast, which is below the day-6 level of the control model (i.e., CAM).

Lin et al. (2006) comment that the IPCC models demonstrating a high level of persistence in the rainfall events tend to do poorly in MJO simulations. It has been shown that the CAM rainfall is more persistent than that of the observations while the ZMO rainfall is a great deal more episodic and less persistent than that of the observations. ZMO evinces a much stronger MJO signal than CAM out to day 6 of the forecast. This is in line with Lin et al. (2006). However, AM2, which displays a good MJO signal out to day 6, shows the same level of persistence in rainfall as CAM. One possible explanation is that ZMO produces episodic, intense events, which are not highly correlated with the observations but can supply energy to the MJO band. AM2 has events that are more intense than CAM but are well correlated with the observations. The superior timing of the AM2's rain events allows it to maintain the MJO signal.

Lin et al. (2006) mention that the characteristics of the waves generated by the IPCC models indicate that the models consistently have equivalent depths that are too large. This can be the result of the models having an effective static stability that is too large. Raymond (2001) defines the effective static stability as

$$\Gamma_{\text{eff}}(z) = \frac{\partial \theta}{\partial z} - \frac{\partial S_\theta}{\partial w}, \quad (3)$$

where  $S_\theta$  is the potential temperature source produced by the diabatic parameterizations,  $\theta$  is the potential temperature,  $z$  is the height, and  $w$  is the vertical velocity. The value of  $\partial S_\theta / \partial w$  is estimated by fitting a line to the  $S_\theta$  and  $w$  data for each level. The slope of this line is taken as the estimate of  $\partial S_\theta / \partial w$ . The effective static stability attempts to quantify the effect of latent heat release to diminish the negative buoyancy associated with large-scale vertical ascent. Figure 16 shows the plots of  $\partial \theta / \partial z$ ,  $\partial S_\theta / \partial w$ , and  $\Gamma_{\text{eff}}(z)$  for the observations, CAM, ZMO, and AM2 at the IFA averaged over the whole TOGA COARE period. As can be seen the  $\Gamma_{\text{eff}}(z)$  profiles indicate that the model values are consistently larger than the observed. Since the initial state is specified, the  $\partial \theta / \partial z$  curves are approximately the same, as the models have not drifted too far. As Lin et al. (2006) surmised, it is the underestimate of  $\partial S_\theta / \partial w$  that drives the differences in  $\Gamma_{\text{eff}}(z)$ . AM2 yields values that are in best agreement with the observations. At least in this case, the models with the lower values of  $\Gamma_{\text{eff}}(z)$  do a bit better in maintaining the MJO amplitude. AM2 appears to have the greatest fidelity to many

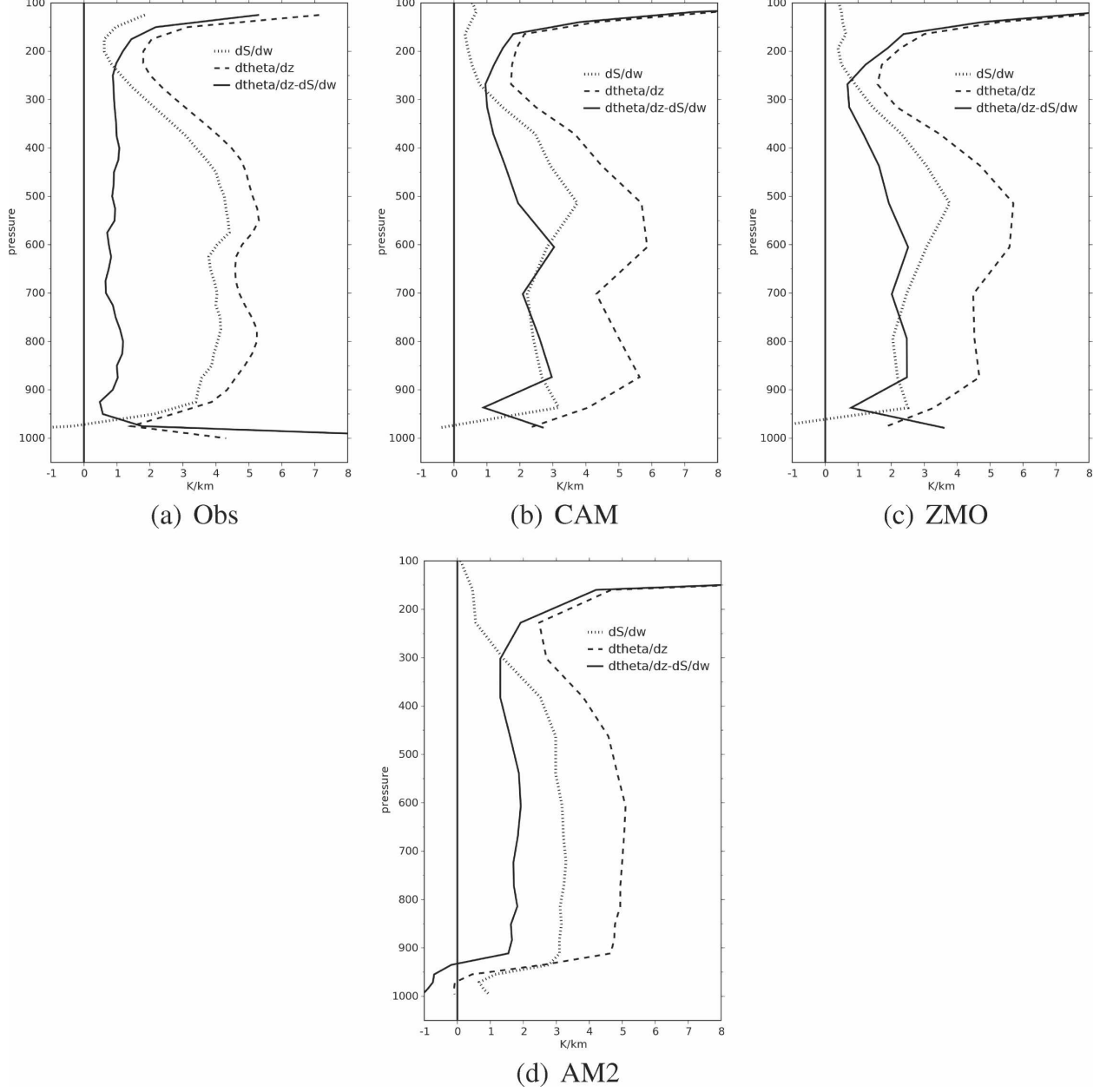


FIG. 16. Profiles of effective static stability ( $\text{K km}^{-1}$ ),  $\Gamma_{\text{eff}}(z)$ , (solid),  $\partial S_{\theta}/\partial w$  (dotted), and  $\partial \theta/\partial z$  (dashed) at the IFA for the (a) observed, (b) CAM, (c) ZMO, and (d) AM2.

physical characteristics that maintain the MJO; this overcomes some of its shortcomings, such as weak heating.

Figure 17 displays a time-pressure diagram of the bandpass-filtered (30–70 day) apparent heat source  $Q_1$  for the observations and the models. This figure shows aspects of the heating profiles related to MJO forcing that can be obscured by time-averaged profiles of Figs. 5 and 6. Of particular interest is the event centered on

21 December 1992. This time coincides with the maximum in observed rainfall at the IFA. In Fig. 17 the observations have a maximum at about 450 hPa at this time. Both CAM and AM2 generally underestimate the magnitude of the  $Q_1$  and especially do for the 21 December event. ZMO has a substantially larger magnitude than the other two models, but its heating on this time scale is not very discriminating, with strong extrema occurring where only weak are observed. Also

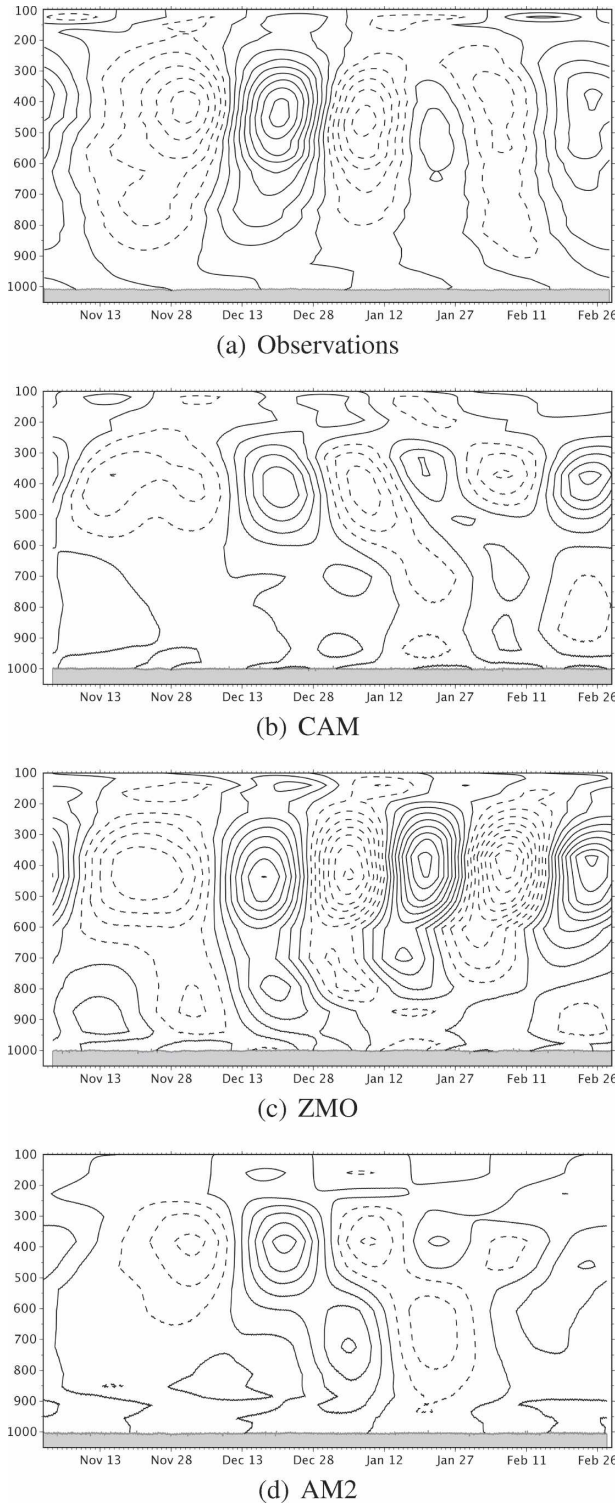


FIG. 17. Bandpass (30–70 days) apparent heat source ( $Q_1$ ) at the IFA. (top to bottom) Observational estimate, CAM forecast day 3, ZMO forecast day 3, and AM2 forecast day 3. Contours are  $0.5 \text{ K day}^{-1}$ . Dashed lines are negative. Zero and positive values are solid lines.

the ZMO maximum in heating occurs about 4 days ahead of the observed, while that in other models coincide almost exactly with the observations. Note that in the developing phase before 21 December, heating begins at the lower levels and afterward, in the decaying phase, the heating ceases more uniformly with height. This picture is in line with the findings of Lin et al. (2004). The models have the opposite slope, with low-level heating occurring after 21 December in the decaying phase. AM2 is the only model with low-level heating in the developing phase, although it is somewhat less organized than in the observations. The contributions to the heating by radiation, convection, and large-scale process were examined for the models. In both CAM and ZMO the convection was very dominant for the 21 December event. In AM2 the convection was dominant, but there was a significant contribution to upper-level heating and low-level cooling by the large scale during the MJO passage. AM2 had features that were quite similar to those estimated from observations by Lin et al. (2004). It would appear the lack of amplitude in the heating in AM2 can be partially compensated by a more accurate placement of the heating in the vertical (Fig. 6), thus maintaining the circulation as seen in Fig. 11. It should be noted that Zhang and Mu (2005), using the convective parameterization of ZMO, observe low-level convective heating preceding the MJO events diagnosed in coupled climate integrations. Apparently, the model running without constraint can achieve more realistic aspects than when it is driven by observed fields. This indicates that the forecast technique needs to be used with other diagnostic methods to fully describe the behavior of any parameterization in a model.

## 7. Conclusions

Using a climate model as a forecast model allows the forcing of specific events. This makes model assessment more exacting regarding parameterizations than using statistics from a climatology. The following conclusions are drawn from results of forecasts over the TOGA COARE period, using CAM3.1, the CAM3.1 modified ZM parameterization, and AM2:

- CAM rains too often and produces rain events of insufficient intensity. The AM2 precipitation at the IFA has similar characteristics, although it has stronger rain events than CAM away from the IFA.
- The CAM model has very little activity in the Indian Ocean, a shortcoming common to many AGCMs (Waliser et al. 2003).
- CAM's rainfall persistence, low level of maximum

- heating, and increased effective stability are all factors noted by Lin et al. (2006) as being detrimental to a successful MJO representation in the models. ZMO and AM2 have better characteristics in this aspect.
- CAM is unable to sustain the observed MJO intensity over a 6-day forecast. This indicates that the poor MJO characteristics of the climate simulations are not due to poor representations of longer time-scale air-sea interactions or radiative processes.
  - The Zhang modification to the CAM's deep convective parameterization results in a stronger, more realistic MJO and time distribution of precipitation. The rainfall events, although as intense as observed, are not consistently produced with the same timing as the observations.
  - AM2 maintains a fairly realistic MJO. The IFA rainfall events are not much more intense than CAM. The AM2 heating profile has a peak higher than that of CAM, but it has a smaller amplitude. This might indicate that the level rather than the magnitude of the heating is a critical factor.
  - Westerly wind bursts are systematically underestimated by all versions of CAM at the IFA. Increasing the number of model levels in the CAM PBL does not address this problem. This bias over the IFA is largely due to CAM missing the westerly wind bursts associated with the two MJO events during the period. The underestimate of the westerly wind is also evident in the CAM climate simulations. ZMO also has a poor representation of these wind events, but for a different reason. CAM fails to capture the shift of precipitation from west to east of the IFA as the MJO propagates. The forcing driven by the convective heating is much the same for all phases of the MJO. ZMO does capture the sense of the precipitation shift, but consistently overestimates the rainfall over land to the west of the IFA and does not have a smooth progression to the east.
  - The effective static stability  $\Gamma_{\text{eff}}$  is overestimated by all the models, with AM2 having values closest to observed estimates.
  - Overall, AM2 appears to have the best simulation of the models and variables considered here.
  - The inclusion of some type of limiter imposed on the deep convective scheme appears to substantially improve the representation of convective events in the tropics. CAM has no such limiters while both AM2 and ZMO do.

**Acknowledgments.** The ERA-40 data were obtained from the Data Support Section of the Scientific Computing Division at the National Center for Atmospheric Research. Joey Comeaux of the NCAR DSS provided

invaluable support. Interpolated OLR and NOAA OI SST V2 data provided by the NOAA/OAR/ESRLPSD, Boulder, Colorado (from their Web site at <http://www.cdc.noaa.gov/SSM/I> data) are produced by the Remote Sensing Systems and are sponsored by the NASA Earth Science REASoN DISCOVER Project. (Data are available at [www.remss.com](http://www.remss.com).) Robert Pincus at the NOAA/Earth System Research Laboratory facilitated the running of the AM2 integrations. Jerry Olson at NCAR provided assistance in implementing modifications of the ZM convection in CAM3.1. Xiaoqing Wu of Iowa State University very generously supplied the code for his modifications to CAM. This work was performed under the auspices of the U.S. Department of Energy (DOE) Office of Science, Biological, and Environmental Research (BER) program by the University of California, Lawrence Livermore National Laboratory, under Contract W-7405-Eng-48. The authors also thank the U.S. Department of Energy, Climate Change Prediction Program (CCPP), Atmospheric Radiation Measurement Program (ARM), and the CCPP-ARM Parameterization Testbed (CAPT).

## REFERENCES

- Agudelo, P. A., J. A. Curry, C. D. Hovas, and P. J. Webster, 2006: Transition between suppressed and active phases of intraseasonal oscillations in the Indo-Pacific warm pool. *J. Climate*, **19**, 5519–5530.
- Ciesielski, P. E., R. H. Johnson, P. T. Haertel, and J. Wang, 2003: Corrected TOGA COARE sounding humidity data: Impact on diagnosed properties of convection and climate over the warm pool. *J. Climate*, **16**, 2370–2384.
- Collins, W. D., and Coauthors, 2004: Description of the NCAR Community Atmosphere Model (CAM 3.0). NCAR Tech. Note NCAR/TN-464+STR, Boulder, CO, 214 pp.
- Fillion, L., H. L. Mitchell, H. Ritchie, and A. Staniforth, 1995: The impact of a digital filter finalization technique in a global data assimilation system. *Tellus*, **47A**, 304–323.
- GFDL Global Atmospheric Model Development Team, 2004: The new GFDL global atmosphere and land model AM2-LM2: Evaluation with prescribed SST simulations. *J. Climate*, **17**, 4641–4673.
- Gregory, D., R. Kershaw, and P. M. Innes, 1997: Parameterization of momentum transport by convection. II: Tests in single column and general circulation models. *Quart. J. Roy. Meteor. Soc.*, **123**, 1153–1183.
- Gutzler, D. S., G. N. Kiladis, G. A. Meehl, K. M. Weickmann, and M. Wheeler, 1994: The global climate of December 1992–February 1993. Part II: Large-scale variability across the tropical western Pacific during TOGA COARE. *J. Climate*, **7**, 1606–1622.
- Hack, J. J., 1994: Parameterization of moist convection in the National Center for Atmospheric Research Community Climate Model (CCM2). *J. Geophys. Res.*, **99**, 5551–5568.
- Houze, R. A. J., S. S. Chen, D. E. Kingsmill, Y. Serra, and S. E. Yuter, 2000: Convection over the Pacific warm pool in relation to the atmospheric Kelvin–Rossby wave. *J. Atmos. Sci.*, **57**, 3058–3089.

- Johnson, R. H., and P. E. Ciesielski, 2000: Rainfall and radiative heating rates from TOGA COARE atmospheric budgets. *J. Atmos. Sci.*, **57**, 1497–1514.
- Lin, J.-L., B. Mapes, M. Zhang, and M. Newman, 2004: Stratiform precipitation, vertical heating profiles, and the Madden-Julian oscillation. *J. Atmos. Sci.*, **61**, 296–309.
- , M. Zhang, and B. Mapes, 2005: Zonal momentum budget of the Madden-Julian oscillation: The source and strength of equivalent linear damping. *J. Atmos. Sci.*, **62**, 2172–2188.
- , and Coauthors, 2006: Tropical intraseasonal variability in 14 IPCC AR4 climate models. Part I: Convective signals. *J. Climate*, **19**, 2665–2690.
- Lin, X., and R. H. Johnson, 1996: Kinematic and thermodynamic characteristics of the flow over the western Pacific warm pool during TOGA COARE. *J. Atmos. Sci.*, **53**, 695–715.
- Lynch, P., and X.-Y. Huang, 1992: Initialization of the HIRLAM model using a digital filter. *Mon. Wea. Rev.*, **120**, 1019–1034.
- McBride, J. L., and W. M. Frank, 1999: Relationships between stability and monsoon convection. *J. Atmos. Sci.*, **56**, 24–36.
- Mechem, D. B., S. S. Chen, and R. A. Houze Jr., 2006: Momentum transport processes in the stratiform regions of mesoscale convective systems over the western Pacific warm pool. *Quart. J. Roy. Meteor. Soc.*, **132**, 709–736.
- Moorthi, S., and M. J. Suarez, 1992: Relaxed Arakawa–Schubert: A parameterization of moist convection for general circulation models. *Mon. Wea. Rev.*, **120**, 978–1002.
- Otnes, R. D., and L. Enochson, 1978: *Applied Time Series Analysis*. Vol. 1. *Basic Techniques*, John Wiley and Sons, Inc., 449 pp.
- Rajendran, K., and A. Kitoh, 2006: Modulation of tropical intraseasonal oscillations by ocean–atmosphere coupling. *J. Climate*, **19**, 366–391.
- Raymond, D. J., 2001: A new model of the Madden–Julian oscillation. *J. Atmos. Sci.*, **58**, 2807–2819.
- Reynolds, R., N. Rayner, T. Smith, D. Stokes, and W. Wang, 2002: An improved in situ and satellite SST analysis for climate. *J. Climate*, **15**, 1609–1625.
- Slingo, J. M., and Coauthors, 1996: Intraseasonal oscillations in 15 atmospheric general circulation models: Results from an AMIP diagnostic subproject. *Climate Dyn.*, **12**, 325–357.
- Tokioka, T., K. Yamazaki, A. Kitoh, and T. Ose, 1988: The equatorial 30–60 day oscillation and the Arakawa–Schubert penetrative cumulus parameterization. *J. Meteor. Soc. Japan*, **66**, 883–901.
- Uppala, S., and Coauthors, 2005: The ERA-40 re-analysis. *Quart. J. Roy. Meteor. Soc.*, **131**, 2961–3012.
- Waliser, D. E., and Coauthors, 2003: AGCM simulations of intraseasonal variability associated with the Asian summer monsoon. *Climate Dyn.*, **21**, 423–446.
- Wentz, F. J., and R. W. Spencer, 1998: SSM/I rain retrievals within a unified all-weather ocean algorithm. *J. Atmos. Sci.*, **55**, 1613–1627.
- White, P. W., Ed., cited 2002: IFS documentation. Part VI: Technical and computational procedures. ECMWF, Shinfield Park, Reading, United Kingdom. [Available online at <http://www.ecmwf.int/research/ifsdocs/CY25r1/index.html>.]
- Wu, X., X.-Z. Liang, and G. J. Zhang, 2003: Seasonal migration of ITCZ precipitation across the equator: Why can't GCMs simulate it? *Geophys. Res. Lett.*, **30**, 1824–1828.
- Xie, P., and A. Arkin, 1997: Global precipitation: A 17-year monthly analysis based on gauge observations, satellite estimates, and numerical model outputs. *Bull. Amer. Meteor. Soc.*, **78**, 2539–2558.
- Zhang, G. J., and N. A. McFarlane, 1995: Sensitivity of climate simulations to the parameterization of cumulus convection in the Canadian Climate Centre general circulation model. *Atmos.–Ocean*, **33**, 407–446.
- , and M. Mu, 2005: Simulation of the Madden–Julian oscillation in the NCAR CCM3 using a revised Zhang–McFarlane convection parameterization scheme. *J. Climate*, **18**, 4046–4064.